

1 **Abstract**
2
3

4 Experiment and simulation were performed to investigate buoyant methane/air
5
6 inverse diffusion flames, with emphasis on the near-field flow dynamics under
7
8 non-reacting and reacting conditions. In the non-reacting flow, the initial shear flow
9
10 and the buoyancy effect induce opposite-direction vortices, which interact with each
11
12 other and cause flow instability similar to the mechanism forming the von Karman
13
14 vortex street. The instability is greatly intensified at around unity Richardson number,
15
16 when the two vortices are comparably strong. In the reacting flows, the density
17
18 gradient is reversed due to chemical heat release and so is the buoyancy-induced
19
20 vortex that it has the same direction with the vortex of the initial shear flow. As a
21
22 result, the buoyancy-induced vorticity generation would facilitate the growth of the
23
24 initial shear layer, thus the near-field flow remains stable. However, the growing shear
25
26 flow would eventually lead to the development of the Kelvin-Helmholtz instability in
27
28 the far field.
29
30
31
32
33
34
35
36
37
38

39 *Keywords:* Inverse Diffusion Flame; Buoyancy; Near-field; Shear flow; Instability.
40
41
42
43
44
45
46
47
48
49
50
51
52
53
54
55
56
57
58
59
60
61
62
63
64
65

1. Introduction

Buoyant diffusion flames exist in a wide range of industrial combustion devices and accidental fires. The research of buoyant diffusion flames is of great significance in optimizing combustion performance, controlling environmental pollution and reducing fire damage. In buoyant diffusion flames, flow instability and laminar-turbulent transition are evident in the near-field where fuel and air mix with each other [1]. The distinct flow and flame dynamics of buoyant diffusion flames have been attributed to combustion heat release, fuel-air density difference, and fuel and air Reynolds numbers [2-4], where the former two are the main factors contributing to the buoyancy effect and greatly influence the flame dynamics at low Reynolds numbers [5].

A number of investigations have been performed to understand the flame or flow instabilities of buoyant normal diffusion flames (NDFs) [6-10], where the flames oscillate at the relatively low frequencies typical of 10-20 Hz [6, 11, 12]. It was also found that the oscillation frequency is slightly affected by the fuel type, the fuel nozzle size, or the fuel inlet velocity [1, 13-17]. Because of the coupling of inertial instability, buoyancy, vortex dynamics, and chemical heat release, it is usually difficult to isolate one factor from another in the study of buoyant NDFs. As a result, the existing literature does not consent on the mechanism of the flow and flame instability in reacting or even non-reacting conditions[18]. Cetegen and Kasper [19] attributed buoyant flow instability to Rayleigh-Taylor instability, but Coats [1] and Buckmaster and Peters [20] to Kelvin-Helmholtz instability. Buckmaster and Peters

1 [20] proposed that the buoyant flow instability is a convective instability that is
2
3 controlled by the thermomechanical properties of the hot and cold gases under the
4
5 gravitational acceleration, but others considered the buoyant flows absolutely unstable
6
7 [21-23]. Jiang and Luo [2, 24-26] studied the formation of large vortex structures in
8
9 buoyant reactive plumes and found that the enhanced tendency of flow transition to
10
11 turbulence in buoyant NDFs is due to combustion induced buoyancy, in contrast to
12
13 the re-laminarization effect of chemical exothermicity in non-buoyant NDFs.
14
15
16
17
18
19

20 Inverse diffusion flames (IDFs), where oxidizer is surrounded by fuel in contrast
21
22 to fuel being surrounded by air in NDFs, have been extensively investigated in
23
24 laboratory with emphasis on soot formation [27-30]. However, to the authors'
25
26 knowledge, relatively limited research attention was focused on the flow and flame
27
28 dynamics in IDFs. Santoro et al. [31] assumed that the flow field in IDFs is similar to
29
30 that of NDFs, in which air co-flow entrainment dominates the near-field of the flame
31
32 base and results in a radial inflow from the side of the main injection together with a
33
34 vertical buoyant flow. Blevins et al. [32] gave a schematic of the IDF flow field,
35
36 where the inward flow in the near-field has a slight expansion, resulting in a small
37
38 radial out flow after a short distance of development. By using laser Doppler
39
40 velocimetry, Kang et al. [33] found that the air flow in IDF tends to move outward to
41
42 the fuel side. Shaddix and Williams [34] provided the velocity field data for ethylene
43
44 IDFs and used the velocity data for soot formation analysis. Recently, Sen et al. [35]
45
46 adopted dynamic systems analysis to understand the connection between flame
47
48 dynamics and thermoacoustic characteristics of a ducted IDF. In spite of these worthy
49
50
51
52
53
54
55
56
57
58
59
60
61
62
63
64
65

1 studies, limited details were provided on the flow or flame oscillation of IDFs in most
2
3 literature.
4

5
6 In their early study, Wu and Essenhigh [36] gave a detailed map for the structure
7
8 of methane IDFs. They found that, with a very low fuel inlet velocity ($< 1\text{cm/s}$), the
9
10 IDFs started to oscillate with a frequency of 1-2 Hz, probably because of the
11
12 relatively important buoyancy effect. Katta et al. [37] investigated the dynamics of an
13
14 IDF, for which the main focus was on the role of flow dynamics in the
15
16 polycyclic-aromatic-hydrocarbon (PAH) and soot formation. According to their
17
18 simulation results, the advection of vorticities at 17.2 Hz enhanced the mixing of the
19
20 species and contributed to a more uniform distribution of PAH in the downstream. In
21
22 both works, no further analysis was provided to address the flame or flow dynamics
23
24 of the IDF, e.g. the main factor determining the instability.
25
26
27
28
29
30
31

32
33
34 IDFs have been recently adopted in synthesizing carbon nanotubes (CNTs) [38,
35
36 39], for which an unstable flow may deactivate the catalyst particles by the
37
38 transportation of polycyclic aromatic hydrocarbons(PAH) or soot to the catalytic
39
40 substrate, thus impeding the growth or degrading the purity of CNTs [40]. Since flow
41
42 exerts an important influence on soot formation of IDFs [29, 34] and flow instability
43
44 may cause difficulty to accurate soot sampling [28, 41], it is necessary to understand
45
46 the IDFs from the flow dynamics perspective [31-33, 36].
47
48
49
50
51

52
53 In the present study, the non-reacting and reacting flows of methane/air IDFs
54
55 were examined through both experiment and numerical simulation. Particle Image
56
57 Velocimetry (PIV) system was used for the measurement of non-reacting flows. Large
58
59
60
61
62
63
64
65

1 eddy simulation (LES), which has been sufficiently validated by the PIV experiment,
2
3 was applied to analyse the unsteady flow and flame dynamics. The main goal of the
4
5 study is to explore the fundamental physics responsible for the flow and flame
6
7 oscillations in buoyant IDFs. The structure of the paper is organized as follows.
8
9 Experimental facilities are described in Section 2, followed by experimental
10
11 observations of flow and flame oscillation in Section 3 and the specifications of the
12
13 present LES in Section 4. Results and detailed discussions for the non-reacting and
14
15 reacting flows are provided in Section 5 and 6, respectively.
16
17
18
19
20
21
22
23
24

25 **2. Experimental Specifications**

26
27 In the present work, a co-annular burner consisting of two concentric
28
29 stainless-steel tubes was built up to generate IDFs, similar to that used by Sidebotham
30
31 and Glassman [41]. As shown in Fig. 1, the air flow is injected through the central
32
33 tube with a diameter of 10 mm and a length of 200 mm, and the fuel flow is injected
34
35 through the annulus between the outer tube and the central tube. The tip of the central
36
37 tube is sharpened to 0.3 mm thickness to reduce the blockage effect that causes wake.
38
39 The upper segment of the central tube is encircled by the outer tube, which has an
40
41 inner diameter of 40 mm, a thickness of 15 mm, and a length of 150 mm. To create a
42
43 uniform inflow velocity profile for the injecting fuel, the annulus is filled with steel
44
45 wire gauze and small steel beads which was also adopted by Sidebotham and
46
47 Glassman [41]. To isolate the flames from the ambient oxygen, a quartz glass tube is
48
49
50
51
52
53
54
55
56
57
58
59
60
61
62
63
64
65

1 installed above the burner to serve as a chimney. The tube has the same diameter as
2
3 the outer burner tube with a length of 300 mm.
4
5

6 The air flow is supplied by a compressed air tank, which has a capacity of 320 L
7
8 and a maximum working pressure of 18.9 bar. A central air supply system is used to
9
10 deliver air to the tank while maintaining pressure. Pure methane (purity 99.9%) stored
11
12 in Dewar tanks is released to provide the fuel flow. Pressure control valves and flow
13
14 meters are combined to control and monitor air and fuel flow rates. The laboratory
15
16 conditions for all the present experiments were 293 K and 101 kPa.
17
18
19
20
21

22 PIV measurement was employed to obtain the non-reacting flow field
23
24 information and hence to validate the present LES results. A schematic of the PIV
25
26 system is shown in Fig. 1 (b), where the IDF burner is mounted vertically. The fuel
27
28 flow is injected directly into the outer annulus, whereas the air flow is pre-mixed with
29
30 PIV particles in a separate tank before entering the central air tube. A Quantel dual
31
32 cavity Nd:Yag laser (EverGreen 600 mJ/pulse, 532 nm wavelength) is used to
33
34 generate laser pulses at 5 Hz. The point laser beam is transformed into a plane laser
35
36 sheet through a series of sheet forming optics. By adjusting the angle of the mirror
37
38 placed above the burner, the laser sheet is aligned with the axis of the burner to enable
39
40 the flow measurement in the xy -plane, as shown in Fig. 1 (b). A TSI Incorporated™
41
42 9307-6 aerosol generator is applied to generate olive oil droplets of 1 μm diameter to
43
44 seed the air flow. The PIV images are captured by a high-speed camera (Hisense 4M,
45
46 2048 \times 2048 pixels), which is synchronized with a Berkeley Nucleonics Corporation
47
48 575 pulse/delay generator, and the time delay between two frames is fixed at 200 μs .
49
50
51
52
53
54
55
56
57
58
59
60
61
62
63
64
65

1 The spatial resolution for the present PIV measurement is 37 pixels/mm. The PIV
2
3 images are processed by the Dantec Dynamic Studio software to obtain the
4
5 corresponding velocity data.
6
7

8
9 For visualizing the reacting IDFs, the flow and flame images are captured using a
10
11 digital camera (Nikon D5200) and a lens (Tamaon 1800mm Macro 1:1). The aperture
12
13 is adjusted to f5.6 and the IOS value was fixed at 1000 to reduce the interference of
14
15 external light. The exposure time for flame image is 1/10 seconds for all of the flame
16
17 images in the present work.
18
19
20
21
22
23
24

25 **3. Experimental Observations of Flow and Flame Oscillation**

26
27 The first experimental evidence for oscillation of IDFs was reported by Wu and
28
29 Essenhigh [36], who found that with sufficiently low fuel velocity the IDFs would
30
31 become unsteady and start to oscillate. Following their observation, we reproduced a
32
33 series of oscillating IDFs and present the instantaneous flame images for a
34
35 representative case in Fig. 2. To characterize the air and fuel inlet flows, we defined
36
37 two Reynolds numbers by
38
39
40
41
42
43

$$44 \quad Re_i = \frac{\rho_i v_i d_i}{\mu_i}, \quad Re_o = \frac{\rho_o v_o d_o}{\mu_o}, \quad (1)$$

45
46 where ρ , v , and μ are the density, velocity, and viscosity; the subscripts i and o
47
48 represent the properties for the air and fuel flows; d_i and d_o are the inner diameters
49
50 of the center air tube and the outer fuel tube. For the IDF in Fig. 2, the air inlet
51
52 velocity is $v_i=30\text{cm/s}$ ($Re_i = 192$) and the fuel inlet velocity is $v_o=2\text{cm/s}$
53
54 ($Re_o = 46$). It is observed that flame oscillation only occurs in the upper portion (i.e.
55
56
57
58
59
60
61
62
63
64
65

1 the yellow cap) of the flame, where the direction of the flame tip swings and the
2
3 height varies, while the blue region at the bottom remains stable.
4
5

6 To understand the source of flame oscillation, we also examined the non-reacting
7
8 flow characteristics for comparison. Here, the non-reacting flow refers to the one with
9
10 the same flow conditions as Fig. 2 but without ignition. Fig.3 shows the instantaneous
11
12 non-dimensional vorticity ($\tilde{\Omega}_z$) contour obtained from the PIV measurement for the
13
14 non-reacting flow, hereinafter, the non-dimensional vorticity is defined as $\tilde{\Omega}_z = \frac{\Omega_z}{2v_i/d_i}$.
15
16 It is seen that the flow is also highly unsteady as the shear layer between fuel and air
17
18 wiggles and deforms dramatically. Qualitatively, the non-reacting flow seems to be
19
20 more unstable than the reacting flow as the bottom half of the shear layer also tends to
21
22 be unsteady. Further justification for this observation will be provided in Sections 5
23
24 and 6. In short, based on the instantaneous flame images in Fig. 2 and the vorticity $\tilde{\Omega}_z$
25
26 contours in Fig. 3, the flow oscillations in both IDFs and their non-reacting flows are
27
28 experimentally confirmed.
29
30
31
32
33
34
35
36
37
38
39
40
41

42 **4. Numerical Methodology and Validation**

43
44 Large eddy simulation (LES), with its advantage in capturing unsteady flow
45
46 motion and relatively cheap computational expense compared to Direct Numerical
47
48 Simulation (DNS), was implemented through the open source code OpenFOAM
49
50 (version 2.3.0) in the present work [42]. Pressure and momentum correctors were
51
52 combined with the Pressure Implicit with the Splitting of Operators (PISO) method
53
54 [43] to solve the time-dependent Navier-Stokes equations. The discretization of
55
56
57
58
59
60
61
62
63
64
65

1 unsteady terms was performed using a second order backward scheme [44]. The
2
3 Normalized Variable Diagram (NVD) scheme (Gamma differencing scheme) [45, 46]
4
5 and the second order central difference scheme were used to discretize the convection
6
7 and diffusion terms. Second order central difference linear interpolation was applied
8
9 for mass flux calculation. The time step was constrained by the
10
11 Courant-Friedrichs-Lewy (CFL) number for stable simulation. The CFL number was
12
13 0.4 for the simulation of non-reacting flow and 0.3 for reacting flow.
14
15
16
17
18
19

20 The infinitely fast and irreversible chemical reaction scheme suffices to
21
22 investigate the present problem. For the present flow-controlled IDFs, the reactants
23
24 are transported to the reaction zone by means of convection and diffusion, the time
25
26 scales of which are much larger than those of chemical reactions. Under the
27
28 conventional assumption of infinitely fast reaction for intensely-burning diffusion
29
30 flames [4], the fuel and the oxidizer react instantaneously when they come in contact
31
32 at the flame that can be therefore treated as a thin sheet. This assumption has been
33
34 widely applied in the research of diffusion flames including buoyant diffusion flames
35
36
37
38
39
40
41
42 [2, 47].
43
44

45 The 3D computational domain and mesh are shown in Fig. 4. Local refinement
46
47 was performed to accurately resolve the unsteady flow near the center of the burner.
48
49 The mesh in Fig. 4 contains 0.5 million grid nodes with all mesh edge size in the
50
51 range of $0.01d_i - 0.12d_i$. Tab. 1 illustrates the boundary conditions for the
52
53 benchmark reacting case presented in Fig. 2. To determine the temperature boundary
54
55 condition on the side wall, the temperature at different vertical locations of the glass
56
57
58
59
60
61
62
63
64
65

1 tube was measured experimentally. As the standard deviation is only about 37K, the
2
3 averaged value of 450K was used in the present simulation for simplicity.
4
5

6 The non-reacting flow presented in Fig. 3 was adopted as a benchmark case to
7
8 validate the present LES. Fig. 5 presents the normalized time-averaged streamwise
9 velocity as a function of span-wise coordinate at different streamwise locations, where
10
11 $\tilde{U}_y = U_y/v_i$ with U_y being the streamwise velocity and $v_i = 30\text{cm/s}$. It is seen
12
13 that the simulation results are in good agreement with experiment, suggesting that the
14
15 adopted flow solver together with the simulation set-up is capable of predicting the
16
17 non-reacting flow field. The grid independence research was performed and the
18
19 results for the cases with grid nodes number of 0.3 million, 0.5 million and 0.7 million,
20
21 which are indicated as Sim. 0.3 M, Sim. 0.5M and Sim. 0.7M respectively, are shown
22
23 in Fig. 5. The convergence of the simulation results of different meshes confirms that
24
25 the grid nodes number of 0.5 million is sufficient for the non-reacting case.
26
27
28
29
30
31
32
33
34
35

36 For the corresponding IDF flow shown in Fig. 2, the validation and the
37
38 grid-dependence analysis of the present LES is unavailable because of the lack of
39
40 velocity measurement. We however noted that the Reynolds number decreases due to
41
42 heat release hence a larger turbulence length scale ($\sim Re^{-1/2}$)[48] is expected.
43
44 Consequently, the mesh for the non-reacting flow is sufficiently fine for its
45
46 corresponding reacting flow, and thus the mesh with grid number of 0.5 million were
47
48 used for the simulation of IDFs.
49
50
51
52
53
54

55 Considering the flame height is one of the most important flame characteristics
56
57 of a non-premixed flame [49-52], we validated the present LES of IDF by comparing
58
59
60
61
62
63
64
65

1 the calculated flame height with the experimental value, as shown in Fig. 6.
 2
 3 According to Mikofski et al. [30], the edge of the blue flame approximates the
 4
 5 reaction zone of methane IDFs, where massive heat is released to cause a local peak
 6
 7 of temperature. In this respect, the outer boundary of the blue flame on the left side of
 8
 9 Fig. 6 approximately matches with the ridge of the temperature contour on the right,
 10
 11 verifying the good agreement between simulation and experiment.
 12
 13
 14
 15
 16
 17
 18
 19

20 **5. Flow Instability of Non-reacting Flows**

21
 22 In a previous study, Jiang and Luo [2] have demonstrated that the
 23
 24 buoyancy-induced vorticity formation owing to the interaction between gravity and
 25
 26 horizontal density gradient is the main cause of the flow instability in reacting plumes.
 27
 28 Noting that the same mechanism also exists in non-reacting plume with horizontal
 29
 30 density gradient and to promote the understanding of flame oscillation in IDF, we
 31
 32 started with analyzing the oscillation of a non-reacting flow in the IDF configuration.
 33
 34
 35
 36
 37
 38

39 For the present axisymmetric incompressible flow, the vorticity transport
 40
 41 equation can be expressed in the non-dimensional form by
 42

$$43 \frac{D\boldsymbol{\omega}}{Dt} = \frac{\rho_a d_i}{\rho^2 u_{ref}^2} (\nabla\rho \times \boldsymbol{g}) + Re^{-1} \nabla^2 \boldsymbol{\omega}, \quad (2)$$

44 where ρ_a is the gas density of the ambient environment, ρ is the local gas density,
 45
 46 \boldsymbol{g} is the gravitational acceleration, d_i is the diameter of the center air tube, and u_{ref}
 47
 48 is a reference velocity. In Eq. 2, the second term quantifies the vorticity diffusion,
 49
 50 which does not generate new vorticity but only changes the vorticity distribution of
 51
 52 the existing flow. Thus, the true source of vorticity is the first term, which produces
 53
 54
 55
 56
 57
 58
 59
 60
 61

1 non-zero vorticity by the non-parallel vertical gravity and horizontal density gradients.

2
3 We further realized that the strength (γ) of a shear layer can be obtained by integrating
4
5
6 vorticity along the normal direction (n) of the shear layer as $\gamma = \int \omega dn$. Thus, the
7
8
9 total change of strength of the buoyancy-induced shear layer (γ_B) can be calculated by
10
11
12 integrating Eq. 2 as

$$13 \frac{d\gamma_B}{dt} = \int_0^{d_o/2} \frac{D\omega}{Dt} dr = \int_{\rho_i}^{\rho_o} \frac{-\rho_a g d_i}{\rho^2 u_{ref}^2} d\rho = \frac{\rho_a g d_i}{u_{ref}^2} \left(\frac{1}{\rho_o} - \frac{1}{\rho_i} \right). \quad (3)$$

14
15
16 Here, the derivation of Eq. 3 requires zero contribution from the vorticity diffusion
17
18 term, $Re^{-1} \nabla^2 \omega$. Since the net effect of this term is the redistribution of vorticity, we
19
20 only need $\nabla \omega = \mathbf{0}$ at the boundary of the shear layer γ_B so that no external
21
22 vorticity enters the vortex. This condition is readily satisfied for any individual
23
24 vortical structure (γ_B included), for which vorticity gradually vanishes at the
25
26 boundary. At this point, it is interesting to note that the result of Eq. 3 can be
27
28 interpreted as a special Richardson number (Ri) defined by
29
30
31
32
33
34
35

$$36 Ri = \frac{(\rho_i - \rho_o) g d_i}{\bar{\rho} u_{ref}^2}, \quad (4)$$

37
38 where $\bar{\rho} = \frac{\rho_i \rho_o}{\rho_a}$. To quantify the vorticity generation inside the shear layer, we can
39
40 formulate the reference velocity by $u_{ref} = v_o - v_i$, which equals the strength of the
41
42 initial shear layer at the inlet. Consequently, the Richardson number defined in Eq. 4
43
44 measures the buoyancy-induced vorticity generation compared to the strength of the
45
46 initial shear layer.
47
48
49
50
51

52
53 To examine the influence of Ri on flow instability of the non-reacting flow
54
55 concerned, we simulated five different cases with varying buoyancy term but fixed
56
57 initial shear term. The buoyancy term was changed by diluting the fuel flow with
58
59
60
61
62
63
64
65

1 0%-100% air, so the density ratio between the air stream and the diluted fuel stream
2
3 could be adjusted between 1.8 and 1.0, hence the Ri varying from 0.95 to 0
4
5 accordingly. Fig. 7 shows the instantaneous vorticity contours in the xy -plane (bottom)
6
7 and the xz -plane (top) at the axial location of $\tilde{y} = 6$. It is observed that flow in
8
9 xy -plane becomes more unstable as Ri increases from 0 to 0.95. Specifically, the
10
11 initial shear layer between fuel and air tends to lose its stability and starts to oscillate
12
13 in the near-field, under the influence of an external shear layer as the buoyancy effect
14
15 becomes more prominent.
16
17
18
19
20
21

22
23 Alternatively, Ri can be adjusted by fixing the buoyancy term while varying the
24
25 initial shear term. This was done by changing v_o so that Ri varies in the range
26
27 between 0.95 and infinity. Again, in this scenario we simulated five different
28
29 non-reacting flows and presented their instantaneous vorticity contours in Fig. 8. It is
30
31 seen that the shear flows and vortical structures in the near-field all display significant
32
33 unsteady features for the cases of $Ri = 0.95, 1.19,$ and 1.86 . As the Richardson number
34
35 further increases to $Ri = 7.44$, the flow structures in the near field tend to become
36
37 relatively stable. When Ri further increases to infinity, the shear layers in the
38
39 near-field grow into a symmetric steady pattern, indicating the establishment of a
40
41 stable flow.
42
43
44
45
46
47
48

49
50 It has been seen that increasing Ri from zero to infinity would cause the stable
51
52 near-field flow to become unstable and then stable. This non-monotonic influence of
53
54 Ri on flow stability of the non-reacting flows can be quantitatively supported by Fig.
55
56 9, where the time averaged streamwise turbulent kinetic energy, $\frac{1}{2}U_y'^2$, is plotted as
57
58
59
60
61
62
63
64
65

1 a function of axial location in the near-field for different Ri . We indeed observed that
2
3 the unsteadiness of the flow is the strongest as Ri approaches 1.
4
5

6 To understand the non-monotonic effect of Ri on the stability of non-reacting
7
8 flows, we can further unravel the physical meanings of the two contributing terms of
9
10 Ri . According to Eqs. 3 and 4, the buoyancy-effect term produces a vorticity
11
12 proportional to $\nabla\rho \times \mathbf{g}$. For non-reacting flows, the density gradient $\nabla\rho$ is caused
13
14 by the different densities between fuel and air. It is note that the vorticity in the initial
15
16 shear flow is given by $\Omega_z = \left(\frac{\partial U_y}{\partial x} - \frac{\partial U_x}{\partial y}\right)\vec{k} \approx \left(\frac{\partial U_y}{\partial x}\right)\vec{k}$. For the present problem, we
17
18 have $\rho_i > \rho_o$ and $v_i > v_o$, which dictates that $\left(\frac{\partial U_y}{\partial x}\right)\vec{k}$ and $\nabla\rho \times \mathbf{g}$ are always of
19
20 opposite directions, as illustrated in the schematic of Fig. 10. This is partially
21
22 supported by the cases with $Ri \neq 0$ in Figs. 7 and 8, where external shear layers grow
23
24 outside of the initial shear layers with opposite-direction vorticity. We note that this
25
26 opposite-direction shear layer configuration much resembles that for the von Karman
27
28 vortex street. To this end, the buoyancy-induced shear flow and the initial shear flow
29
30 are two competing mechanisms in the near-field of a non-reacting flow. It is important
31
32 to note that the dominance of either of the mechanisms (Ri being either very small or
33
34 very large) would promote flow stabilization in the near-field, although instability
35
36 could still develop in the far field as the nature of the dominant shear flow evolves
37
38 from laminar to turbulent. However, if the two effects are comparable to each other
39
40 (Ri approaches 1), instability would develop immediately from the near-field because
41
42 of the strong interaction between vortices with comparable strengths but of opposite
43
44 signs. This explains why the near-field instability of a non-reacting flow is most
45
46
47
48
49
50
51
52
53
54
55
56
57
58
59
60
61
62
63
64
65

1 significant near $Ri = 1$.
2

3 According to the schematic of the interaction of the two shear flows shown in
4 Fig.10, the instability for non-reacting flow cannot be categorized into the classical
5 Kelvin-Helmholtz instability. Specifically, this instability is similar to that in Karman
6 vortex street since they have the similar vortex sheet configuration. The two shear
7 layers in the Karman vortex street have the same vorticity intensity and therefore are
8 simpler than those in the present problem. To further clarify this statement, the
9 vorticity contour of a zoomed-in region in the near field is shown in Fig.11 (b). The
10 observation of the interaction of the two shear flows indicates that the instability is
11 similar to that in Karman vortex street.
12
13
14
15
16
17
18
19
20
21
22
23
24
25
26

27 Realizing that both the buoyancy-induced vorticity generation and the initial
28 shear flow are not unique to a non-reacting flow in IDF configuration, we were
29 inspired to extend the above understanding of flow instability to non-reacting flows in
30 NDF configuration. A non-reacting flow in NDF configuration was simulated by
31 injecting fuel flow through the center tube with a velocity of 30 cm/s and air flow
32 through the annular with a velocity of 2 cm/s, so that the air/fuel configuration is
33 exactly opposite of the benchmark case presented in Figs. 7 and 8. In this case, the
34 initial shear flow is identical to the non-reacting flow in IDF configuration, and so is
35 the magnitude of the density gradient. However, the notable difference is the direction
36 of the density gradient and consequently the direction of the buoyancy-induced
37 vorticity. The outcome of the difference is that the initial shear flow would be
38 enhanced by the buoyancy-induced vorticity generation in the non-reacting flow in
39
40
41
42
43
44
45
46
47
48
49
50
51
52
53
54
55
56
57
58
59
60
61
62
63
64
65

1 NDF configuration, instead of being counteracted in the non-reacting flow in NDF
2
3 configuration. In this case, the growing initial shear layer would remain stable in the
4
5 near field, until it reaches certain critical Reynolds number and develops
6
7 Kelvin-Helmholtz instability in the far field. This is indeed verified in Fig. 12 by the
8
9 stable and growing shear flow of the NDF. The streamline plots in Fig. 12 also
10
11 confirm the existence of asymmetric vortices in the near-field of the IDF flow,
12
13 indicating a state of unstableness; whereas no individual vortex presents in the
14
15 near-field of the NDF, indicating a state of stableness.
16
17
18
19
20
21

22 Based on the above observation and analysis, it was identified that in
23
24 non-reacting flows: the buoyancy induces shear flows in an opposite direction to the
25
26 initial shear flows; the interaction between the buoyancy induced shear flows and the
27
28 initial shear flows causes instability in the near-field; the flow instability increases as
29
30 the Richardson number is close to unity.
31
32
33
34
35
36
37
38

39 **6. Flame Instability in IDFs**

40
41 To understand the flame instability in IDFs, we recognized that any flow
42
43 instability is the result of unsteady behaviors of vorticity, which should not be
44
45 fundamentally different between reacting and non-reacting flows. Thus, the two
46
47 mechanisms responsible for the instability of the non-reacting flow can be applied to
48
49 the IDF to understand the effect of combustion on flow stability. Fig. 13 illustrates the
50
51 comparison between a non-reacting flow (the benchmark case shown in Fig. 3) and its
52
53 corresponding IDF (shown in Fig. 2) with the same inlet flow conditions. Here, we
54
55
56
57
58
59
60
61
62
63
64
65

1 consider the region containing the flame to be the near-field of the IDF, where the fuel
2 and oxidizer mixes and interacts with each other intensively. It is observed that the
3 initial shear flow of the IDF is notably enhanced in the near-field, because the inner
4 flow velocity is significantly increased as a result of thermal expansion caused by the
5 combustion heat release. Moreover, the density gradient of the IDF is reversed so that
6 the $\nabla\rho \times \mathbf{g}$ term is opposite of that for the non-reacting flow. This is because the
7 combustion heats up the inner flow and hence reduces its density to be lower than that
8 of the outer flow. As a result, the buoyancy-induced vorticity $\nabla\rho \times \mathbf{g}$ and the
9 vorticity $(\frac{\partial U_y}{\partial x})\vec{k}$ of the initial shear flow have the same direction. This shear layer
10 configuration resembles the non-reacting flow in NDF configuration discussed in
11 Section 5, in the sense that the buoyancy effect in both cases would enhance the initial
12 shear flow.

13
14
15
16
17
18
19
20
21
22
23
24
25
26
27
28
29
30
31
32
33
34 Based on the above analysis, we conjectured that the buoyancy effect stabilizes
35 the initial shear flow in the near-field of an IDF. This conjecture is qualitatively
36 supported by the comparison between the non-reacting and reacting flows in Fig. 13,
37 where the shear layer of the reacting flow displays relatively symmetric structure in
38 the near-field compared with the non-reacting flow. For a better illustration, Fig. 14
39 shows the time evolution of the vorticity contour for the non-reacting and reacting
40 flows. Again, stable vortical structures can be observed in the near-field of the IDF,
41 but unstable vortical structures are evident in the near-field of the non-reacting flow.
42 For the non-reacting flow, we can observe additional vorticities outside the initial
43 shear flow but with opposite direction. These vortices are the direct evidence for the
44
45
46
47
48
49
50
51
52
53
54
55
56
57
58
59
60
61
62
63
64
65

1 buoyancy-induced shear flow. As discussed above, the buoyancy-induced shear flow
2
3 and the initial shear flow are comparable to each other but of opposite vorticity, flow
4
5 instability develops immediately in the near-field.
6
7

8
9 For a quantitative validation of the above analysis, Fig. 15 presents the evolution
10
11 of the time-averaged streamwise turbulent kinetic energy evolution along the axial
12
13 direction. The point $(0, \tilde{y} = 3.8, 0)$ is where the time-averaged flame tip is located
14
15 and serves as the indicator for the near-field of the IDF. The result suggests that the
16
17 unsteadiness in the near-field of the IDF is much lower than its non-reacting flow.
18
19 Therefore, we conclude that the combustion-induced buoyancy effect suppresses the
20
21 flow instability in the near-field of IDFs.
22
23
24
25
26
27

28 It should be also noted that the above results imply that the far field of the IDF is
29
30 more unstable than that of its non-reacting flow. This can be understood by that, since
31
32 the initial shear flow is greatly enhanced in the near-field, natural instability
33
34 (Kelvin-Helmholtz) starts to develop in the far field as the critical Reynolds number
35
36 increases. The stronger shear flow of the IDF would induce stronger momentum
37
38 transportation after the instability kicks in, which is reflected by the higher
39
40 unsteadiness of the flow. Similar observation was also reported by Jiang and Luo [2],
41
42 who stated that chemical heat release enhances the flow instability in buoyant flame.
43
44 However, our study clarifies that the flow instability of a buoyant flame should be
45
46 considered separately in the near-field and the far field, the latter of which will be the
47
48 focus of a future work. The above observation of reacting flows can be summarized as
49
50 that the IDF chemical heat release causes a reversed density gradient that suppresses
51
52
53
54
55
56
57
58
59
60
61
62
63
64
65

1 the near field instability.
2
3
4
5

6 **7. Concluding Remarks** 7 8

9 Buoyant methane/air inverse diffusion flames (IDFs) were experimentally and
10 numerically investigated to understand their instability in the near-field. It is found
11 that, in buoyant non-reacting flows, the initial shear flow and the buoyancy effect
12 induce opposite-direction vorticities and the interaction between them causes flow
13 instability in the near-field. The flow instability, measured by the turbulent intensity,
14 increases as Ri approaches unity, at which the buoyancy term equals the initial shear
15 term. Furthermore, chemical reaction would result in an enhancement of the initial
16 shear layer in the near-field and a reversed density gradient, thereby suppressing the
17 near-field flow instability.
18
19
20
21
22
23
24
25
26
27
28
29
30
31
32

33 In the present study, the non-reacting flow simulation has been quantitatively
34 validated by the PIV measurement and enables us to reveal the flow instability caused
35 by the interaction of the initial shear flow and the buoyancy-induced shear flow. The
36 role of the combustion heat release in suppressing the flow instability in the near field
37 was clarified by using the reacting flow simulation with simplified combustion
38 chemistry and transport models. Further quantification of the role requires not only
39 the PIV measurement on the reacting flow but also the LES of the IDF with detailed
40 reaction mechanism and species transport. Although they are unnecessary to be
41 considered in the present study, a further examination of the reacting flow by PIV and
42 LES merits future studies for enriching our understanding on IDFs.
43
44
45
46
47
48
49
50
51
52
53
54
55
56
57
58
59
60
61
62
63
64
65

1 In the present work focused on the flow and flame dynamics of IDFs, chemical
2
3 reaction happens in an “infinitely fast” manner and its detailed process is neglected.
4
5 Moreover, the Peclet number, measuring the relative importance of convection
6
7 compared with diffusion, and on the Lewis number, measuring the relative importance
8
9 of thermal diffusion compared with mass diffusion, were not considered in the study.
10
11 The influence of these factors on the flame structure and flow instability merits future
12
13 studies.
14
15
16
17
18
19

20 Although the present study is focused on investigating the flow instability of
21
22 inverse diffusion flames, the flame-acoustics may play a role by either enhancing or
23
24 suppressing the instability depending on the various factors [53]. It is however
25
26 difficult to make a quantitative evaluation of the flame-acoustic interplay on the
27
28 instability of the present flow through various existing criteria, such as Rayleigh
29
30 criterion [54] or Chu’s criterion [55], where the generation of acoustic wave requires
31
32 the oscillation in heat release. For the present IDFs attached to the tube tip, the mixing
33
34 between fuel and oxidizer in the unstable flow is a potential source for heat release
35
36 perturbation. However, as observed experimentally and numerically, the flow is stable
37
38 in the near downstream of the tube tip, which corresponding to the flame region with
39
40 massive heat release. Thus, the oscillation in heat release is unlikely to be significant
41
42 in the present problem for considering the flame-acoustic interaction, which certainly
43
44 merits future studies.
45
46
47
48
49
50
51
52
53

54 **Acknowledgement**

55
56
57
58
59
60
61
62
63
64
65

1 This work was supported by the Hong Kong RGC/GRF (operating under
2
3 contract numbers PolyU 152217/14E and 152651/16E) and partly by the Hong Kong
4
5
6 Polytechnic University (G-UA2M and G-YBGA).
7
8
9
10

11 **References**

12 [1] C.M. Coats, Coherent structures in combustion, *Prog. Energy Combust. Sci.* 22
13 (1996) 427-509.
14
15
16

17 [2] X. Jiang, K.H. Luo, Dynamics and structure of transitional buoyant jet diffusion
18 flames with side-wall effects, *Combust. Flame* 133 (2003) 29-45.
19
20
21

22 [3] A. Liñán, E. Fernandez-Tarrazo, M. Vera, A.L. Sánchez, Lifted laminar jet
23 diffusion flames, *Combust. Sci. Technol.* 177 (2005) 933-953.
24
25
26

27 [4] A. Liñán, M. Vera, A.L. Sánchez, Ignition, liftoff, and extinction of gaseous
28 diffusion flames, *Annu. Rev. Fluid Mech.* 47 (2015) 293-314.
29
30
31

32 [5] G. Cox, *Combustion fundamentals of fire*, Academic Press(1995).
33
34
35

36 [6] L.D. Chen, J.P. Seaba, W. Roquemore, L. Goss, Buoyant diffusion flames, *Proc.*
37 *Comb. Inst.* 22 (1989) 677-684.
38
39
40

41 [7] W.M.G. Malalasekera, H.K. Versteeg, K. Gilchrist, A review of research and an
42 experimental study on the pulsation of buoyant diffusion flames and pool fires, *Fire*
43 *Mater.* 20 (1996) 261-271.
44
45
46

47 [8] M.R.J. Charest, C.P.T. Groth, Ö.L. Gülder, Effects of gravity and pressure on
48 laminar coflow methane–air diffusion flames at pressures from 1 to 60 atmospheres,
49 *Combust. Flame* 158 (2011) 860-875.
50
51
52

53 [9] T.C. Williams, C.R. Shaddix, R.W. Schefer, P. Desgroux, The response of buoyant
54 laminar diffusion flames to low-frequency forcing, *Combust. Flame* 151 (2007)
55 676-684.
56
57
58

1 [10] A. Datta, Effects of gravity on structure and entropy generation of confined
2 laminar diffusion flames, *Int. J. Therm. Sci.* 44 (2005) 429-440.

3
4
5 [11] B.W. Albers, A.K. Agrawal, Schlieren analysis of an oscillating gas-jet diffusion
6 flame, *Combust. Flame* 119 (1999) 84-94.

7
8
9
10 [12] T. Toong, Mechanisms of combustion instability, *Proc. Comb. Inst.* 10 (1965)
11 1301-1313.

12
13
14 [13] F.A. Williams, *Combustion Theory* 2nd ed., Addison-Wesley, Reading,
15 MA, 1985.

16
17
18
19 [14] E.E. Zukoski, *Properties of fire plumes*, *Combustion Fundamentals of Fire*,
20 Academic Press, San Diego (1995).

21
22
23
24 [15] A.F. Ghoniem, I. Lakkis, M. Soteriou, Numerical simulation of the dynamics of
25 large fire plumes and the phenomenon of puffing, *Proc. Comb. Inst.* 26 (1996)
26 1531-1539.

27
28
29
30 [16] A. Hamins, J.C. Yang, T. Kashiwagi, An experimental investigation of the
31 pulsation frequency of flames, *Proc. Comb. Inst.* 24 (1992) 1695-1702.

32
33
34
35 [17] V.R. Katta, W.M. Roquemore, Role of inner and outer structures in transitional
36 jet diffusion flame, *Combust. Flame* 92 (1993) 274-282.

37
38
39
40 [18] X. Jiang, K.H. Luo, Combustion-induced buoyancy effects of an axisymmetric
41 reactive plume, *Proc. Comb. Inst.* 28 (2000) 1989-1995.

42
43
44
45 [19] B.M. Cetegen, K.D. Kasper, Experiments on the oscillatory behavior of buoyant
46 plumes of helium and helium-air mixtures, *Phys. Fluids* 8 (1996) 2974-2984.

47
48
49
50 [20] J. Buckmaster, N. Peters, The infinite candle and its stability—a paradigm for
51 flickering diffusion flames, *Proc. Comb. Inst.* 21 (1988) 1829-1836.

52
53
54
55 [21] T. Maxworthy, The flickering candle: transition to a global oscillation in a
56 thermal plume, *J. Fluid. Mech.* 390 (1999) 297-323.

57
58
59
60 [22] P. Huerre, P.A. Monkewitz, Local and global instabilities in spatially developing
61

flows, *Ann. Rev. Fluid Mech.* 22 (1990) 473-537.

[23] A. Lingens, K. Neemann, J. Meyer, M. Schreiber, Instability of diffusion flames, *Proc. Comb. Inst.* 26 (1996) 1053-1061.

[24] X. Jiang, K.H. Luo, Spatial direct numerical simulation of the large vortical structures in forced plumes, *Flow Turbulence Combust.* 64 (2000) 43-69.

[25] X. Jiang, K. Luo, Direct numerical simulation of the near field dynamics of a rectangular reactive plume, *Int. J. Heat Fluid Flow* 22 (2001) 633-642.

[26] X. Jiang, K. Luo, Combustion-induced buoyancy effects of an axisymmetric reactive plume, *Proc. Comb. Inst.* 28 (2000) 1989-1995.

[27] A. Sobiesiak, J.C. Wenzell, Characteristics and structure of inverse flames of natural gas, *Proc. Comb. Inst.* 30 (2005) 743-749.

[28] G.W. Sidebotham, I. Glassman, Flame temperature, fuel structure, and fuel concentration effects on soot formation in inverse diffusion flames, *Combust. Flame* 90 (1992) 269-272.

[29] C. Kaplan, K. Kailasanath, Flow-field effects on soot formation in normal and inverse methane-air diffusion flames, *Combust. Flame* 124 (2001) 275-294.

[30] M.A. Mikofski, T.C. Williams, C.R. Shaddix, L.G. Blevins, Flame height measurement of laminar inverse diffusion flames, *Combustion and Flame* 146 (2006) 63-72.

[31] R. Santoro, T. Yeh, J. Horvath, H. Semerjian, The transport and growth of soot particles in laminar diffusion flames, *Combust. Sci. Technol.* 53 (1987) 89-115.

[32] L.G. Blevins, R.A. Fletcher, B.A. Benner, E.B. Steel, G.W. Mulholland, The existence of young soot in the exhaust of inverse diffusion flames, *Proc. Comb. Inst.* 29 (2002) 2325-2333.

[33] K.T. Kang, J.Y. Hwang, S.H. Chung, W. Lee, Soot zone structure and sooting limit in diffusion flames: Comparison of counterflow and co-flow flames, *Combust. Flame* 109 (1997) 266-281.

1 [34] C.R. Shaddix, T.C. Williams, Measurements of the velocity field in laminar
2 ethylene inverse jet diffusion flames, *Combust. Flame* 156 (2009) 942-945.

3
4
5 [35] U. Sen, T. Gangopadhyay, C. Bhattacharya, A. Mukhopadhyay, S. Sen, Dynamic
6 characterization of a ducted inverse diffusion flame using recurrence analysis,
7 *Combust. Sci. Technol.*, (2017).

8
9
10 [36] K.T. Wu, R.H. Essenhigh, Mapping and structure of inverse diffusion flames of
11 methane, *Proc. Comb. Inst.* 20 (1985) 1925-1932.

12
13
14
15 [37] V.R. Katta, L.G. Blevins, W.M. Roquemore, Dynamics of an inverse diffusion
16 flame and its role in polycyclic-aromatic-hydrocarbon and soot formation, *Combust.*
17 *Flame* 142 (2005) 33-51.

18
19
20 [38] F. Xu, X. Liu, D.T. Stephen, Synthesis of carbon nanotubes on metal alloy
21 substrates with voltage bias in methane inverse diffusion flames, *Carbon* 44 (2006)
22 570-577.

23
24
25 [39] G.W. Lee, J. Jurng, J. Hwang, Formation of Ni-catalyzed multiwalled carbon
26 nanotubes and nanofibers on a substrate using an ethylene inverse diffusion flame,
27 *Combust. Flame* 139 (2004) 167-175.

28
29
30 [40] C.J. Unrau, R.L. Axelbaum, P. Biswas, P. Fraundorf, Synthesis of single-walled
31 carbon nanotubes in oxy-fuel inverse diffusion flames with online diagnostics, *Proc.*
32 *Combust. Inst.* 31 (2007) 1865-1872.

33
34
35 [41] G.W. Sidebotham, I. Glassman, Effect of oxygen addition to a near-sooting
36 ethene inverse diffusion flame, *Combust. Sci. Technol.* 81 (1992) 207-219.

37
38
39 [42] H.G. Weller, G. Tabor, H. Jasak, C. Fureby, A tensorial approach to
40 computational continuum mechanics using object-oriented techniques, *Comp. Phys.*
41 12 (1998) 620-631.

42
43
44 [43] R.I. Issa, Solution of the implicitly discretised fluid flow equations by
45 operator-splitting, *J. Comput. Phys.* 62 (1986) 40-65.

46
47
48 [44] H. Jasak, Error analysis and estimation for finite volume method with
49 applications to fluid flow, Ph.D. thesis, Imperial College of Science, Technology
50 and Medicine, 1996.

1 [45] B. Leonard, Simple high - accuracy resolution program for convective modelling
2 of discontinuities, *Int. J. Numer. Methods Fluids* 8 (1988) 1291-1318.

3
4
5 [46] M. Darwish, A new high-resolution scheme based on the normalized variable
6 formulation, *Numer. Heat Transfer Part B* 24 (1993) 353-371.

7
8
9 [47] K. Balasubramanian, R.I. Sujith, Non-normality and nonlinearity in
10 combustion-acoustic interaction in diffusion flames, *J. Fluid Mech.* 594 (2008) 29-57.

11
12
13 [48] M.T. Landahl, E. Mollo-Christensen, *Turbulence and random processes in fluid
14 mechanics*, Cambridge University Press 1992.

15
16
17 [49] A. D'anna, A. D'Alessio, J. Kent, A computational study of hydrocarbon growth
18 and the formation of aromatics in coflowing laminar diffusion flames of ethylene,
19 *Combust. Flame* 125 (2001) 1196-1206.

20
21
22 [50] D.B. Makel, I.M. Kennedy, Soot formation in laminar inverse diffusion flames,
23 *Combust. Sci. Technol.* 97 (1994) 303-314.

24
25
26 [51] J. Du, R.L. Axelbaum, The effect of flame structure on soot-particle inception in
27 diffusion flames, *Combust. Flame* 100 (1995) 367-375.

28
29
30 [52] E.J. Lee, K.C. Oh, H.D. Shin, Soot formation in inverse diffusion flames of
31 diluted ethene, *Fuel* 84 (2005) 543-550.

32
33
34 [53] T. Poinso, D. Veynante, *Theoretical and numerical combustion*, RT Edwards,
35 Inc. 2005.

36
37
38 [54] J.W.S. Rayleigh, *The Theory of Sound, Volume Two*, Dover Publications, Inc.:
39 New York, NY, USA, 1945.

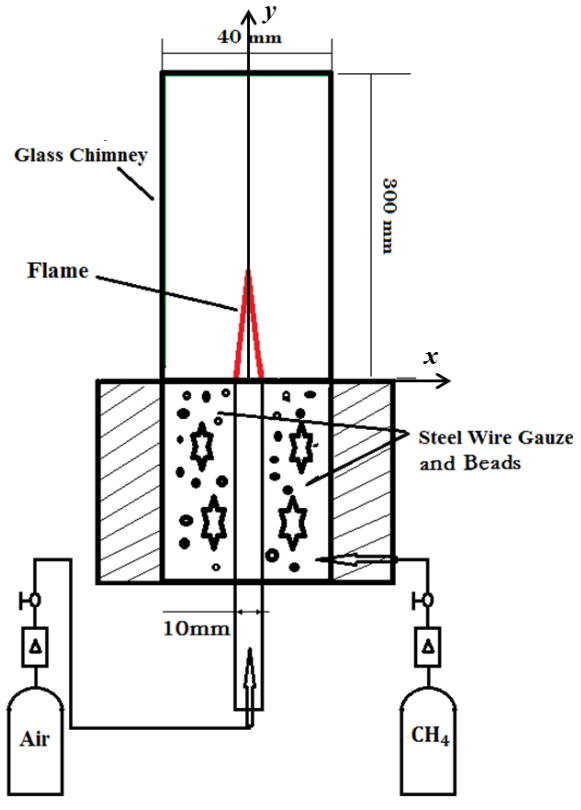
40
41
42 [55] B.-T. Chu, On the energy transfer to small disturbances in fluid flow (Part I),
43 *Acta Mech.* 1 (1965) 215-234.

Table 1: Boundary conditions for the benchmark reacting IDF case

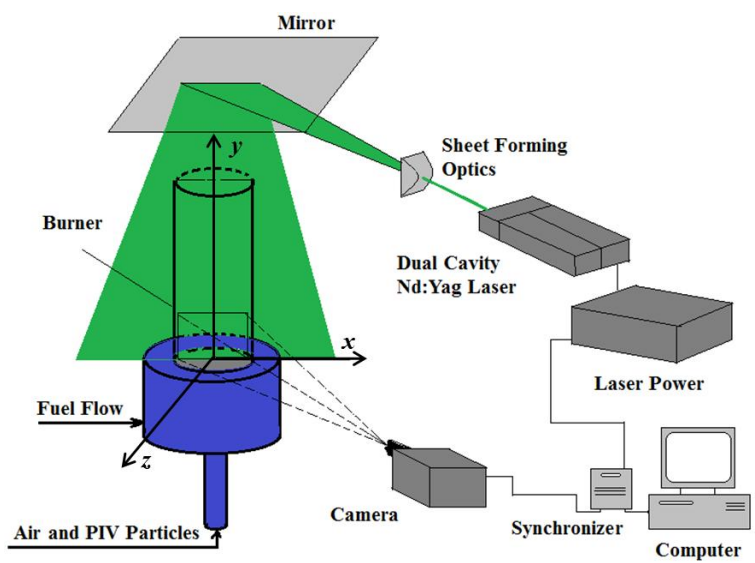
	Velocity (m/s)	Pressure (Pa)	Temperature (K)	Components (-)
Air inlet	0.3	Zero Gradient	300	100% air
Fuel inlet	0.02	Zero Gradient	300	100% Methane
Outlet	Zero Gradient	101325	Zero Gradient	Zero Gradient
Glass chimney	0	Zero Gradient	450	Zero Gradient

1
2
3
4
5
6
7
8
9
10
11
12
13
14
15
16
17
18
19
20
21
22
23
24
25
26
27
28
29
30
31
32
33
34
35
36
37
38
39
40
41
42
43
44
45
46
47
48
49
50
51
52
53
54
55
56
57
58
59
60
61
62
63
64
65

1
2
3
4
5
6
7
8
9
10
11
12
13
14
15
16
17
18
19
20
21
22
23
24
25
26
27
28
29
30
31
32
33
34
35
36
37
38
39
40
41
42
43
44
45
46
47
48
49
50
51
52
53
54
55
56
57
58
59
60
61
62
63
64
65



(a)



(b)

Figure 1: Schematics of (a) the IDF burner and (b) the PIV system.



Figure 2: Instantaneous images of an IDF with $Re_i = 192$ and $Re_o = 46$.

1
2
3
4
5
6
7
8
9
10
11
12
13
14
15
16
17
18
19
20
21
22
23
24
25
26
27
28
29
30
31
32
33
34
35
36
37
38
39
40
41
42
43
44
45
46
47
48
49
50
51
52
53
54
55
56
57
58
59
60
61
62
63
64
65

1
2
3
4
5
6
7
8
9
10
11
12
13
14
15
16
17
18
19
20
21
22
23
24
25
26
27
28
29
30
31
32
33
34
35
36
37
38
39
40
41
42
43
44
45
46
47
48
49
50
51
52
53
54
55
56
57
58
59
60
61
62
63
64
65

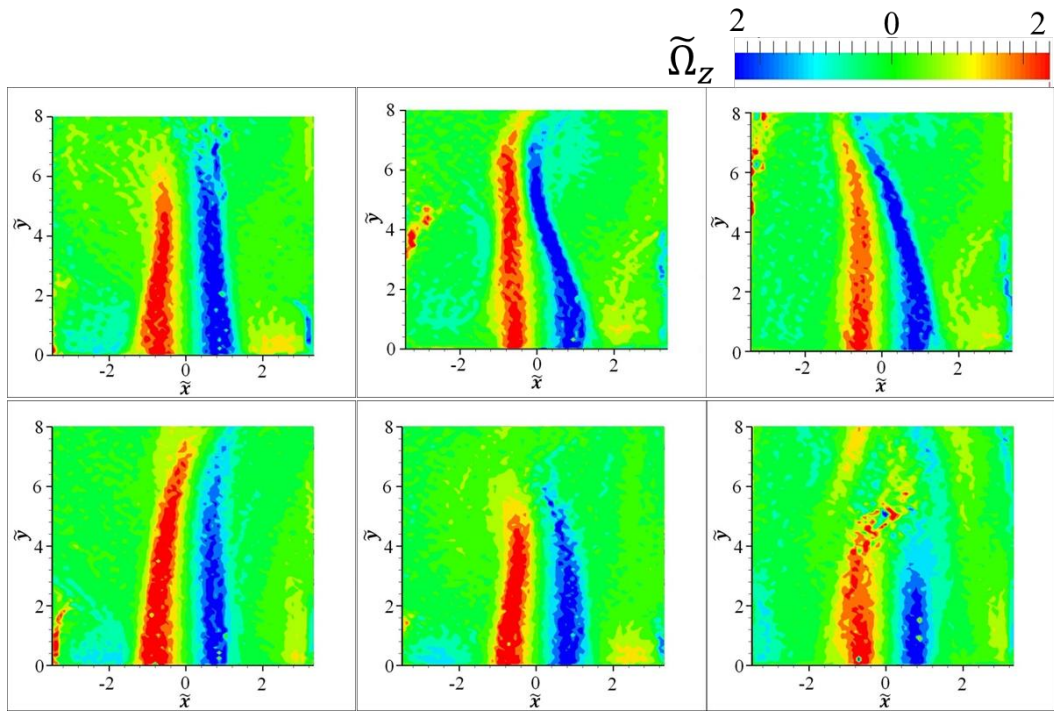


Figure 3: Instantaneous vorticity contours of the non-reacting flow with $Re_i = 192$ and $Re_o = 46$. $\tilde{x} = 2x/d_i$ and $\tilde{y} = 2y/d_i$.

1
2
3
4
5
6
7
8
9
10
11
12
13
14
15
16
17
18
19
20
21
22
23
24
25
26
27
28
29
30
31
32
33
34
35
36
37
38
39
40
41
42
43
44
45
46
47
48
49
50
51
52
53
54
55
56
57
58
59
60
61
62
63
64
65

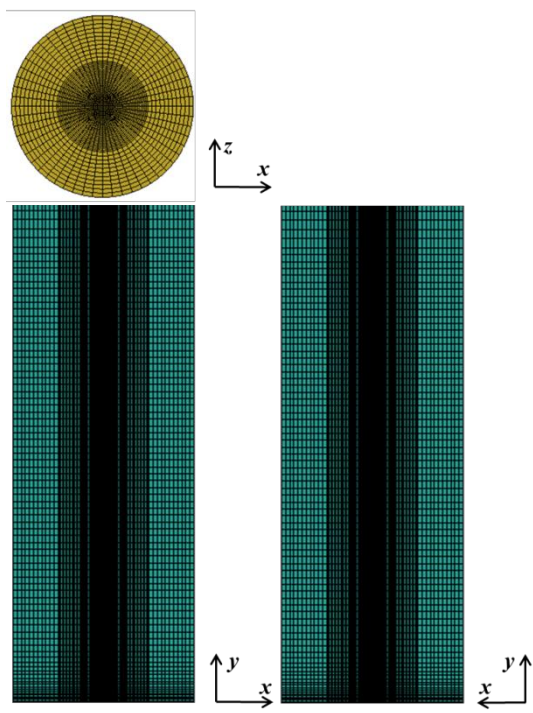


Figure 4: Computational domain and mesh for the present LES.

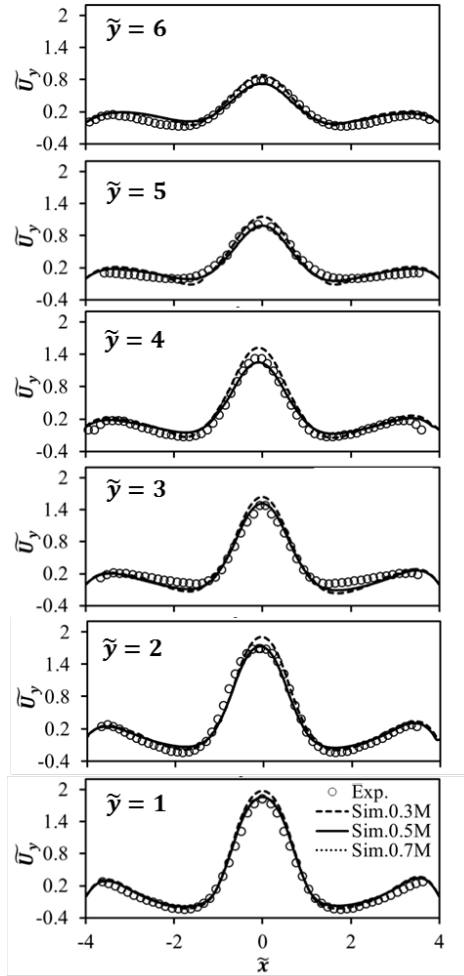


Figure 5: Validation of time-averaged streamwise velocity at different axial locations and grid independence analysis for the benchmark case presented in Fig. 3. Sim.0.3M, Sim.0.5M, and Sim.0.7M denote the simulation results with 0.3million, 0.5 million, and 0.7 million grid nodes, respectively.

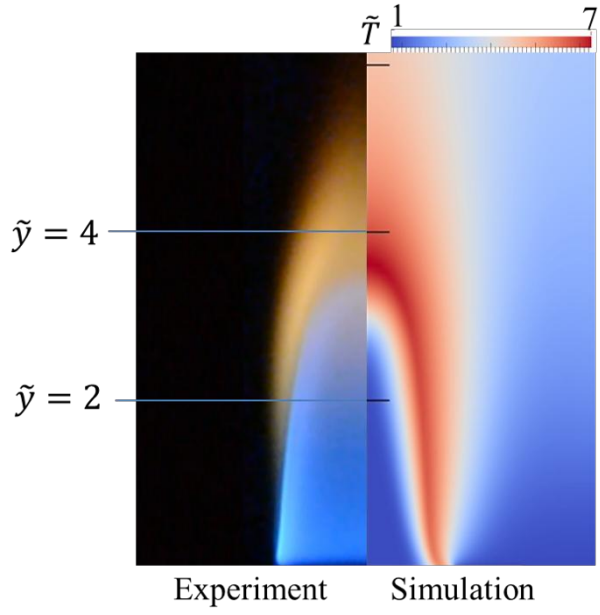


Figure 6: Comparison of flame height between experiment and simulation for the benchmark case of IDF shown in Fig. 2. The non-dimensional temperature is defined as: $\tilde{T} = \frac{T}{T_0}$ with $T_0 = 300K$.

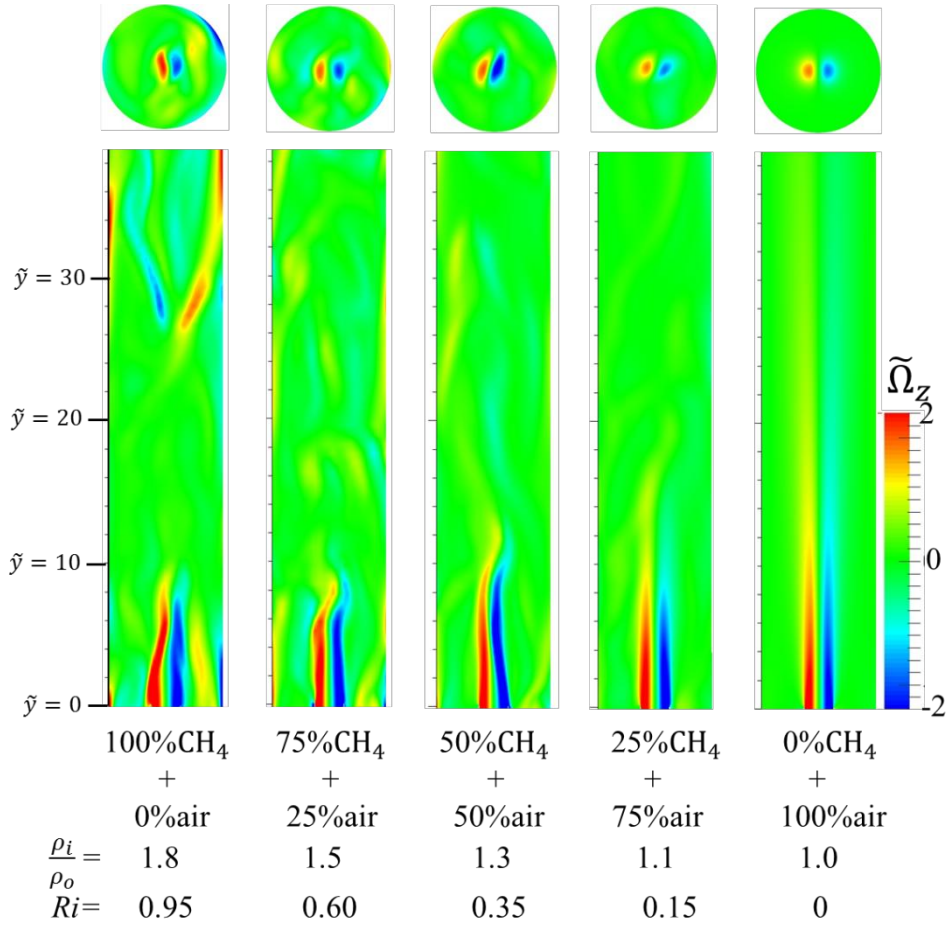


Figure 7: Instantaneous vorticity contours in the xy -plane (bottom) and the xz -plane (top) at $\tilde{y} = 6$. The Richardson number is adjusted by varying the air/fuel density ratio. The first plot corresponds to the benchmark case introduced in Section 3.

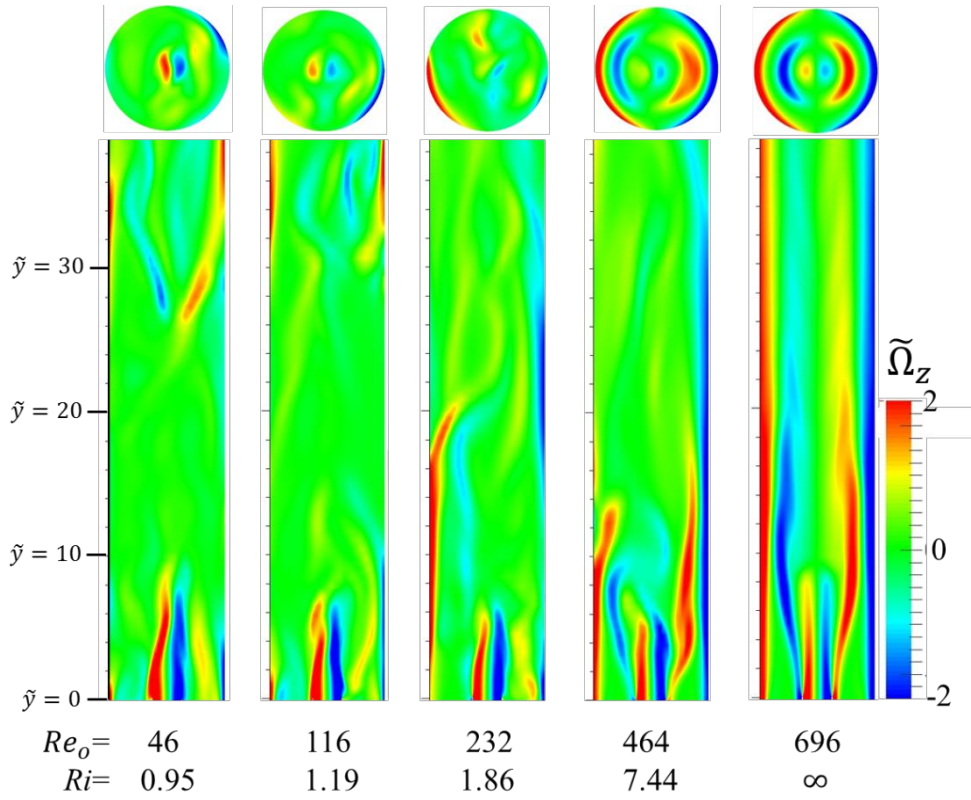


Figure 8: Instantaneous vorticity contours in the xy -plane (bottom) and the xz -plane (top) at $\tilde{y} = 6$. Ri is adjusted by varying the initial shear term through Re_o while fixing the buoyancy term. The first plot corresponds to the benchmark case introduced in Section 3.

1
2
3
4
5
6
7
8
9
10
11
12
13
14
15
16
17
18
19
20
21
22
23
24
25
26
27
28
29
30
31
32
33
34
35
36
37
38
39
40
41
42
43
44
45
46
47
48
49
50
51
52
53
54
55
56
57
58
59
60
61
62
63
64
65

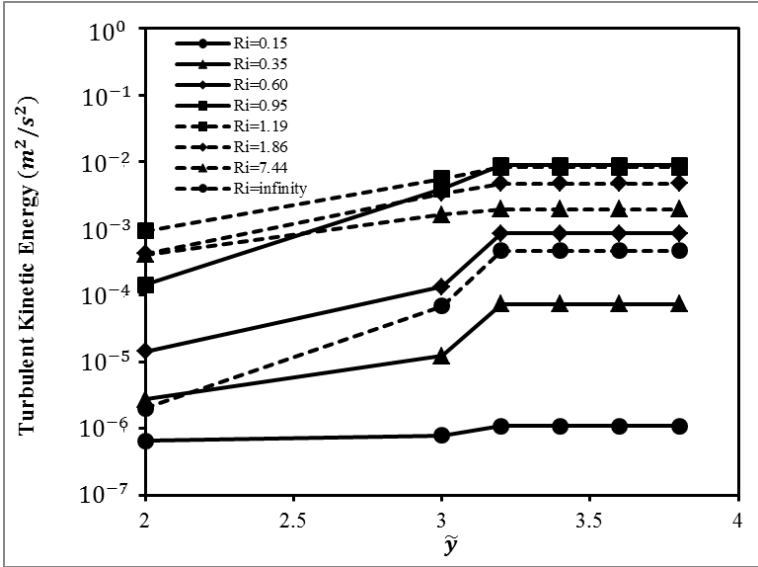


Figure 9: Time-averaged turbulent kinetic energy, $\frac{1}{2}U_y'^2$ at different axial locations for different Ri .

1
2
3
4
5
6
7
8
9
10
11
12
13
14
15
16
17
18
19
20
21
22
23
24
25
26
27
28
29
30
31
32
33
34
35
36
37
38
39
40
41
42
43
44
45
46
47
48
49
50
51
52
53
54
55
56
57
58
59
60
61
62
63
64
65

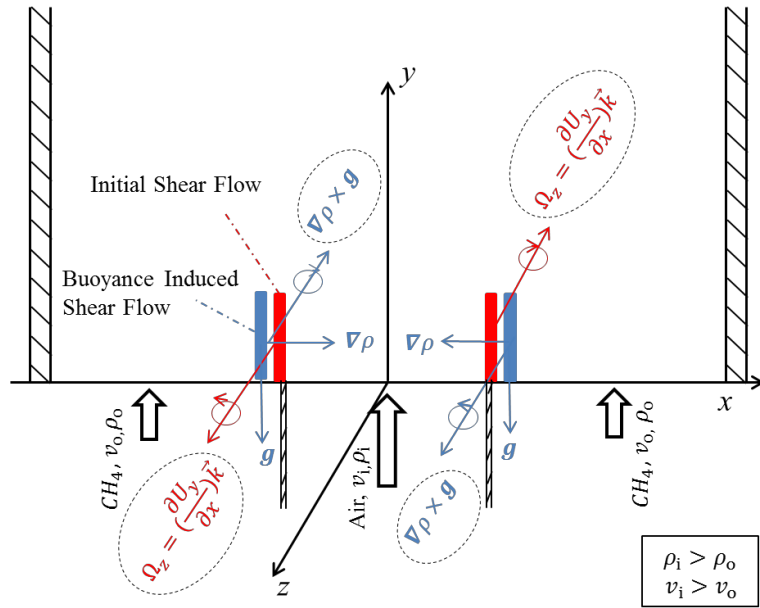


Figure 10: Schematic of the relation between the initial shear flow and the buoyancy-induced shear flow in the near-field of a non-reacting flow.

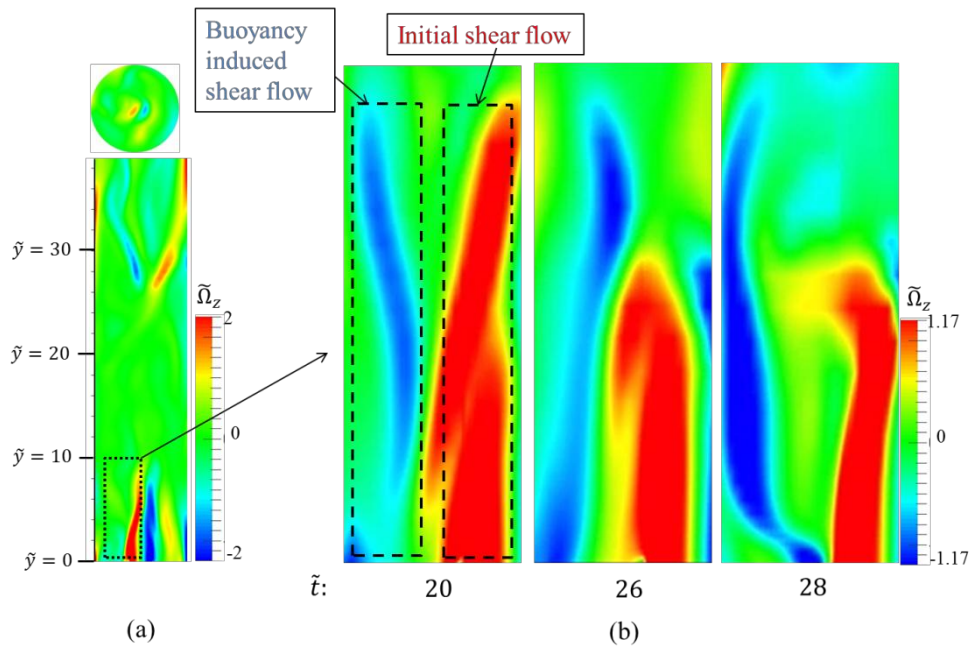


Figure 11. The instantaneous vorticity contours for the benchmark case with $Re_1 = 192, Re_2 = 46$. The non-dimensional time is defined as $\tilde{t} = 2tv_i/d_i$.

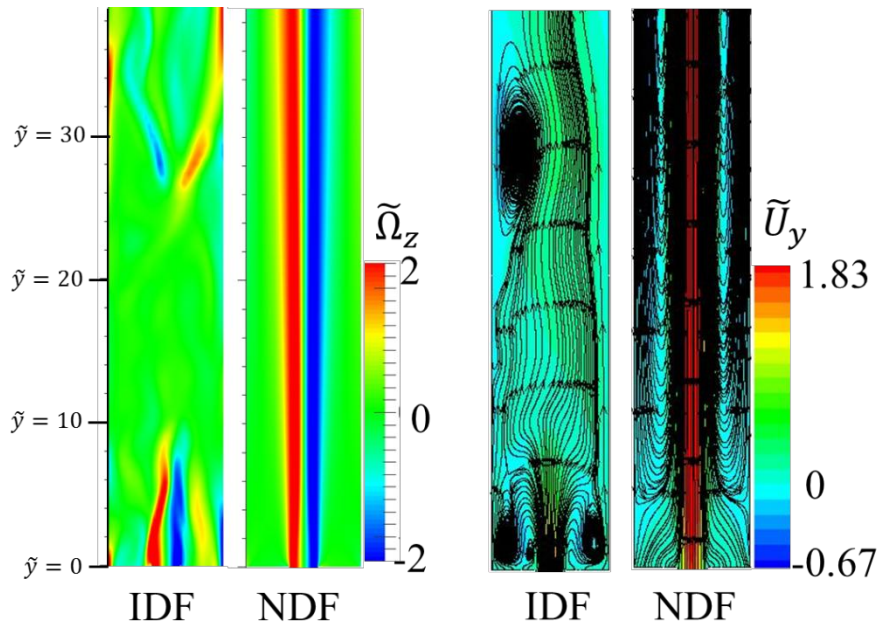


Figure 12: Comparison of the instantaneous vorticity contour (left) and streamline (right) between a non-reacting flow in IDF configuration and a non-reacting flow in IDF configuration.

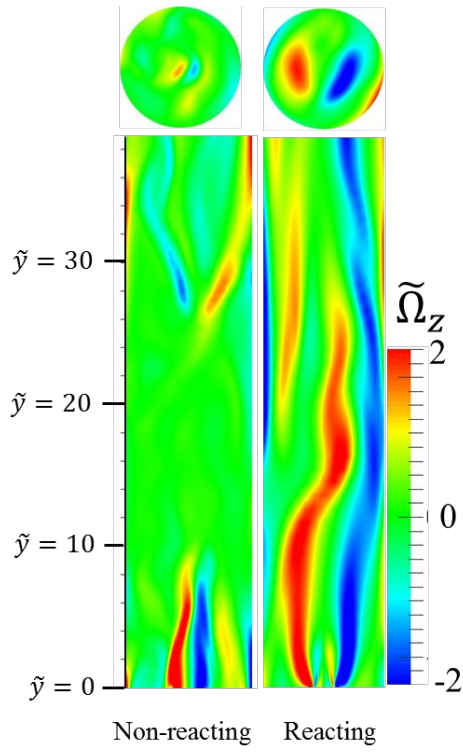
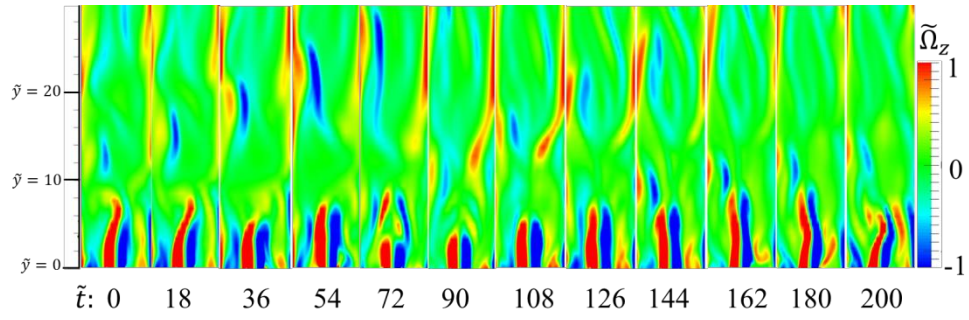
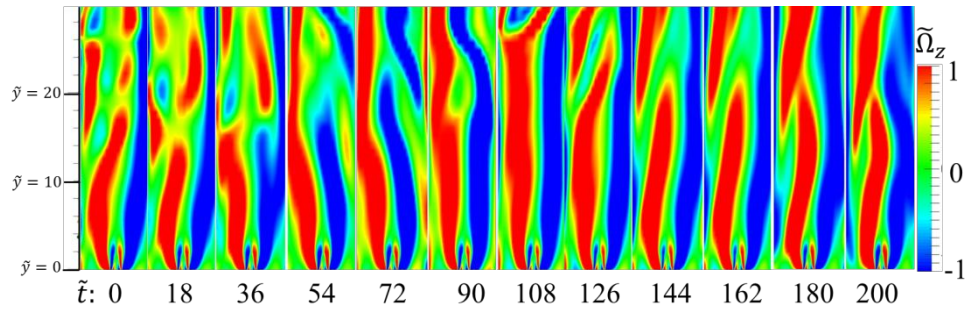


Figure 13: Comparison of the instantaneous vorticity contour between the non-reacting and reacting flows.



(a)



(b)

Figure 14: Time evolution of the vorticity contour for (a) the non-reacting flow and (b) the reacting flow. The non-dimensional time is defined as $\tilde{t} = 2tv_i/d_i$.

1
2
3
4
5
6
7
8
9
10
11
12
13
14
15
16
17
18
19
20
21
22
23
24
25
26
27
28
29
30
31
32
33
34
35
36
37
38
39
40
41
42
43
44
45
46
47
48
49
50
51
52
53
54
55
56
57
58
59
60
61
62
63
64
65

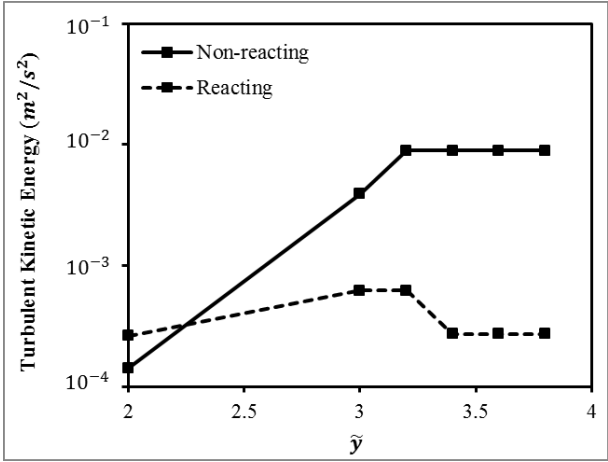
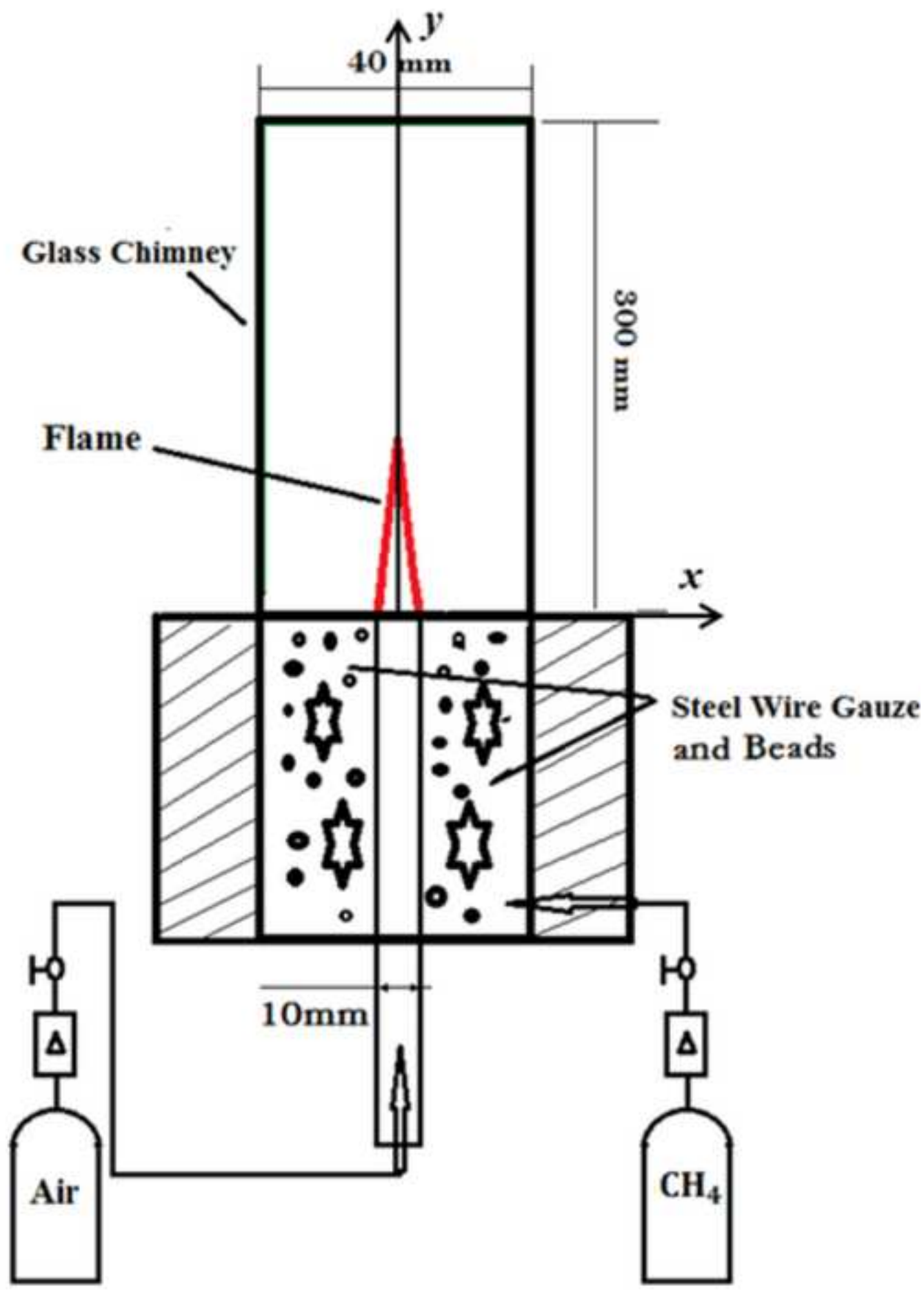


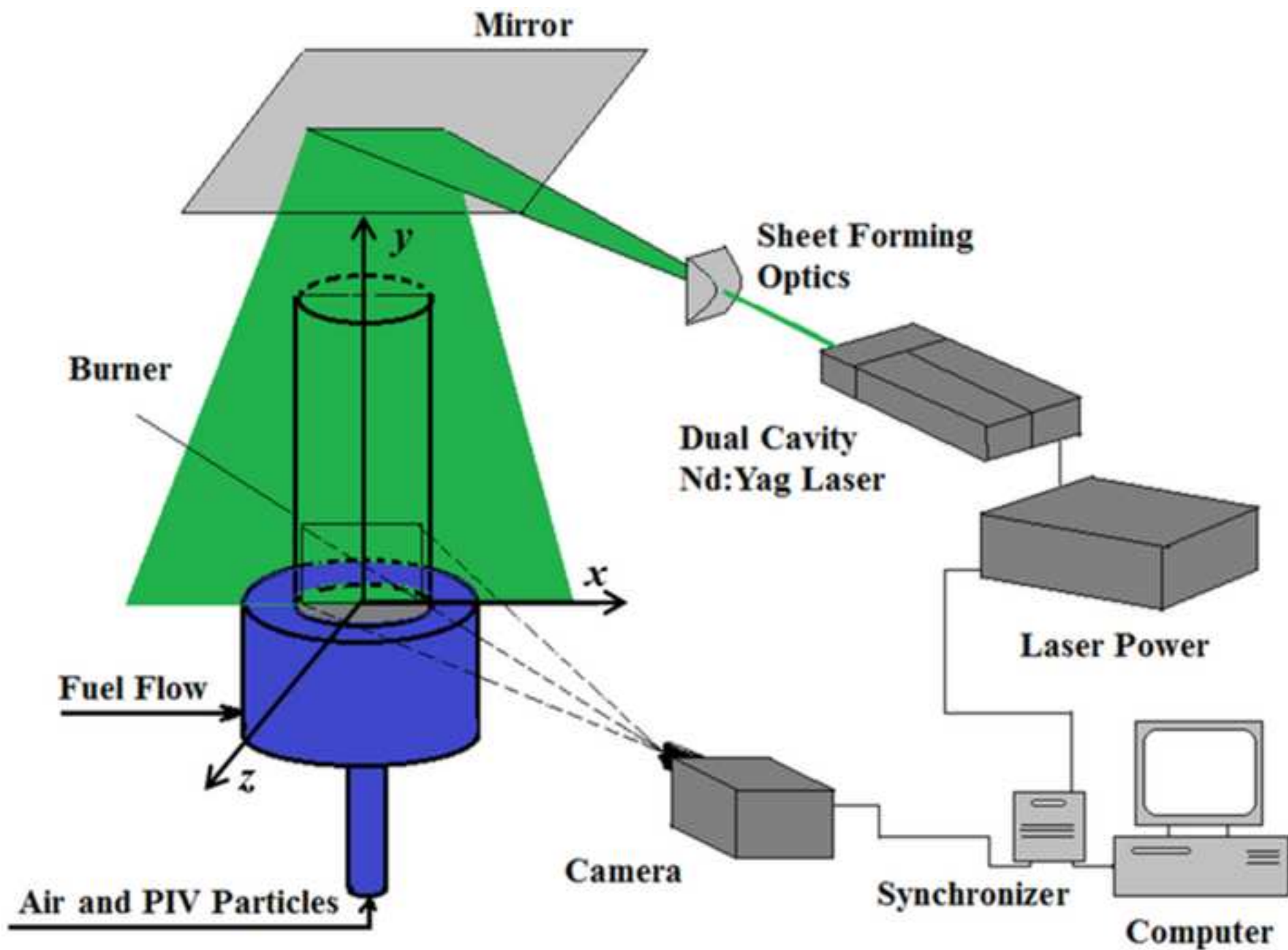
Figure 15: Time-averaged turbulent kinetic energy, $\frac{1}{2}U_y'^2$ for the non-reacting and reacting flows at different axial locations.

Figure
[Click here to download high resolution image](#)



Figure

[Click here to download high resolution image](#)



Figure

[Click here to download high resolution image](#)



Figure
[Click here to download high resolution image](#)

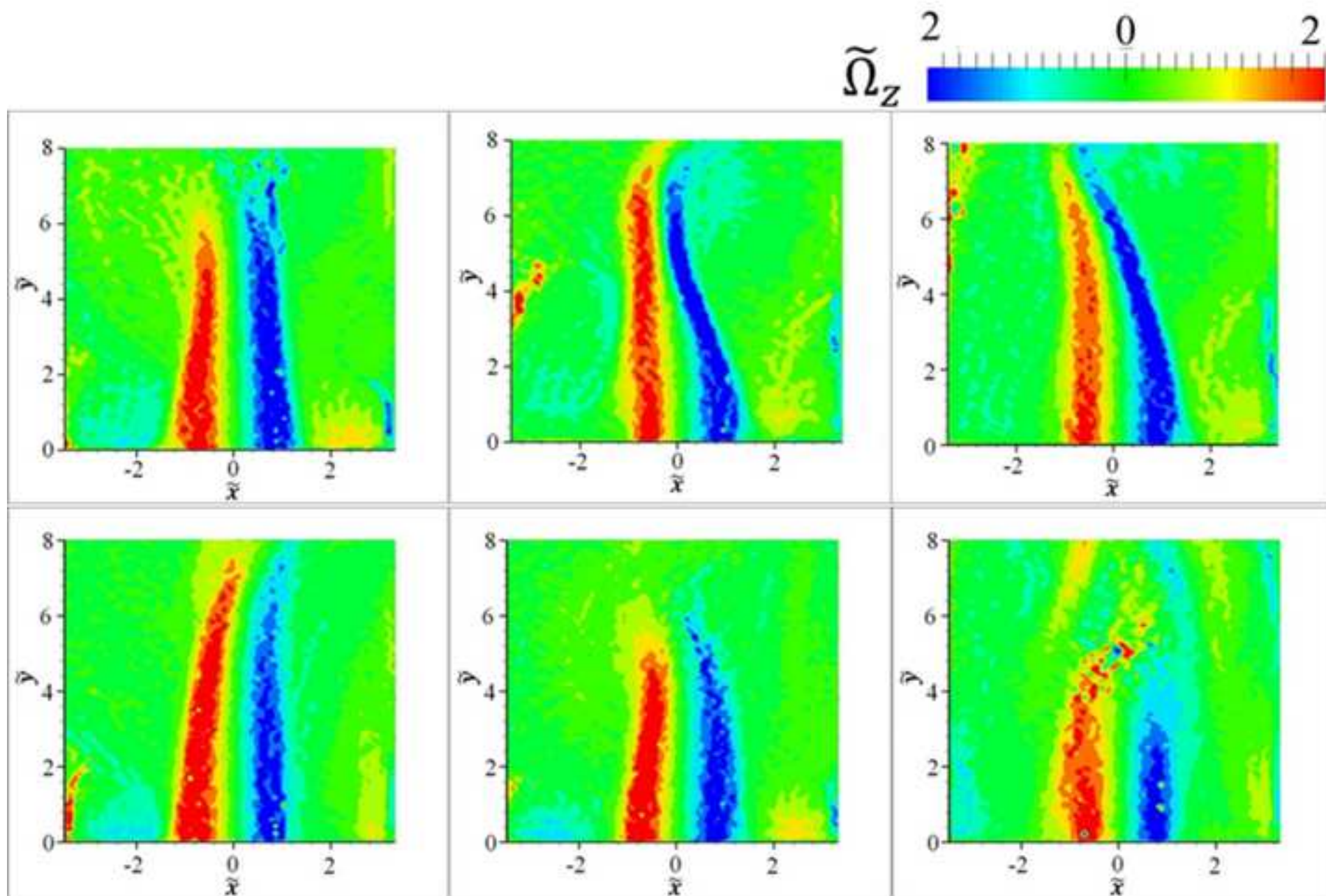
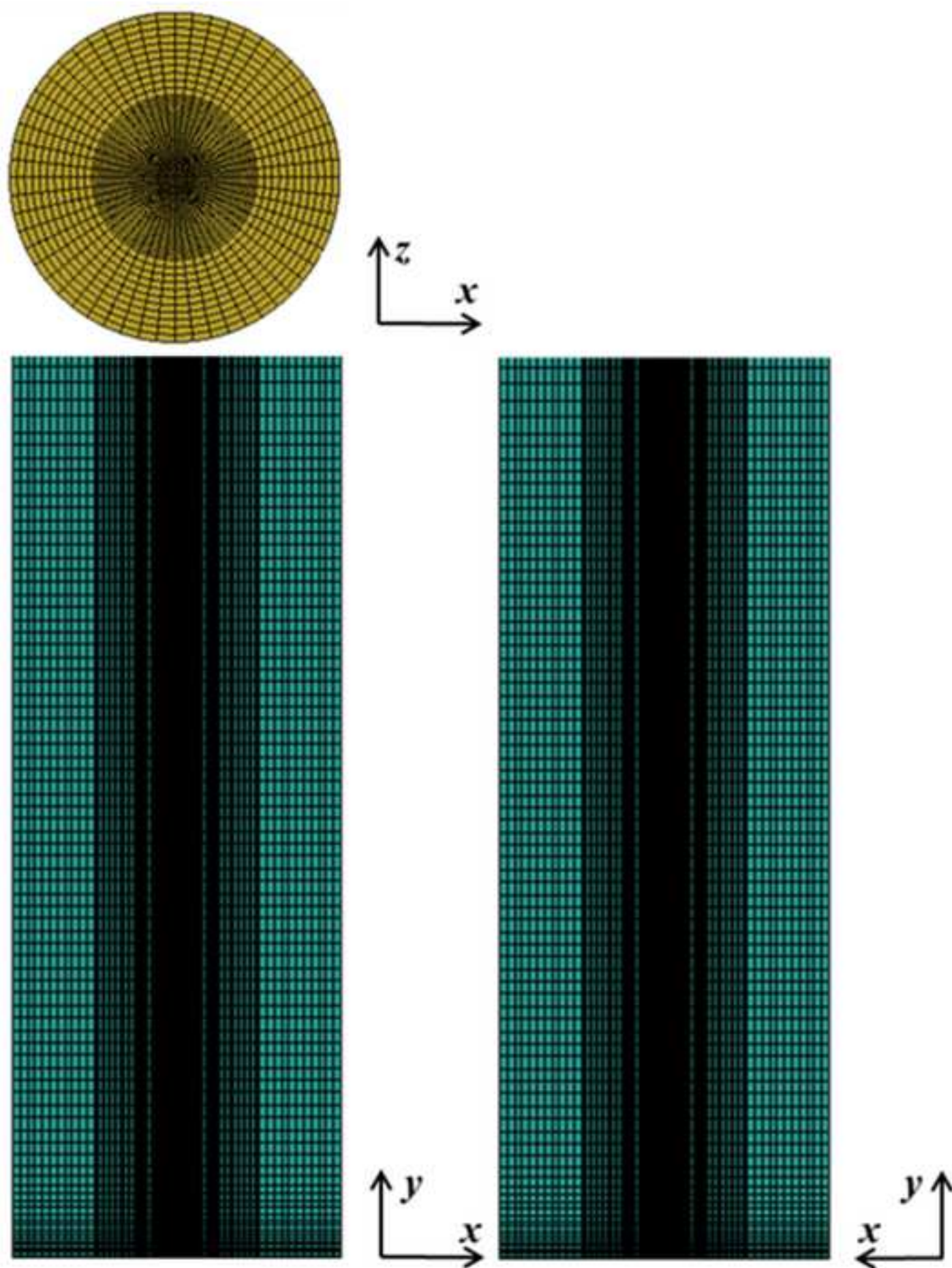
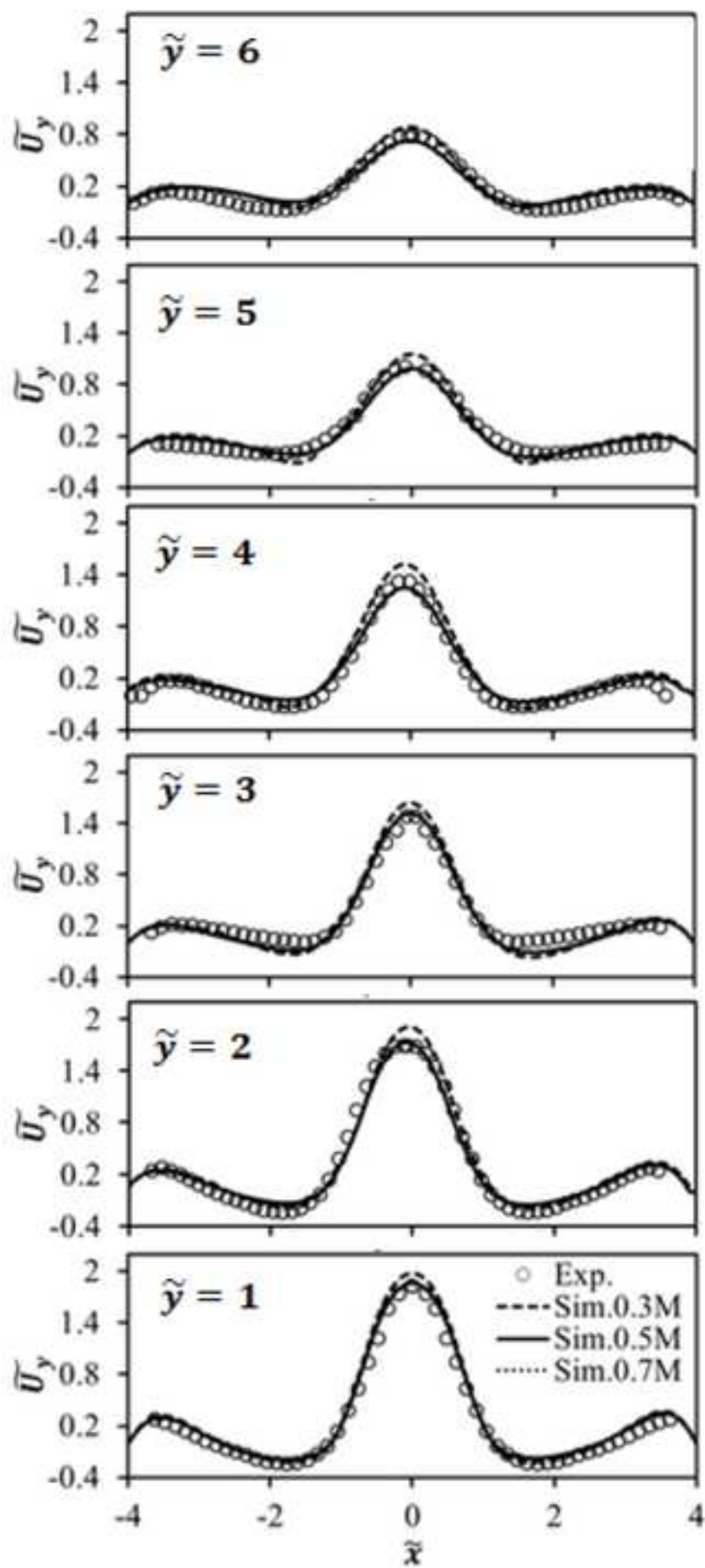
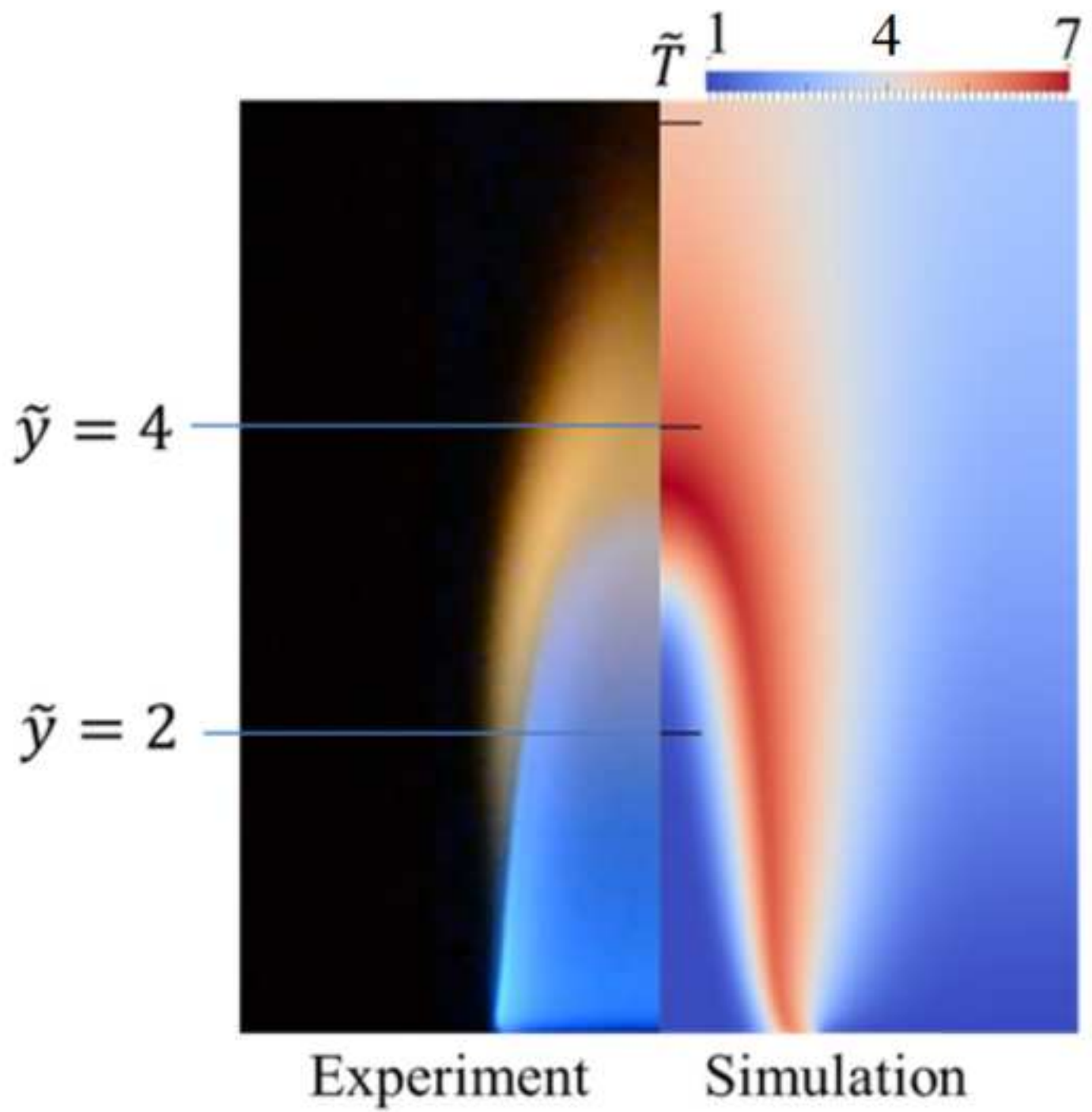


Figure
[Click here to download high resolution image](#)



Figure

[Click here to download high resolution image](#)



Figure

[Click here to download high resolution image](#)

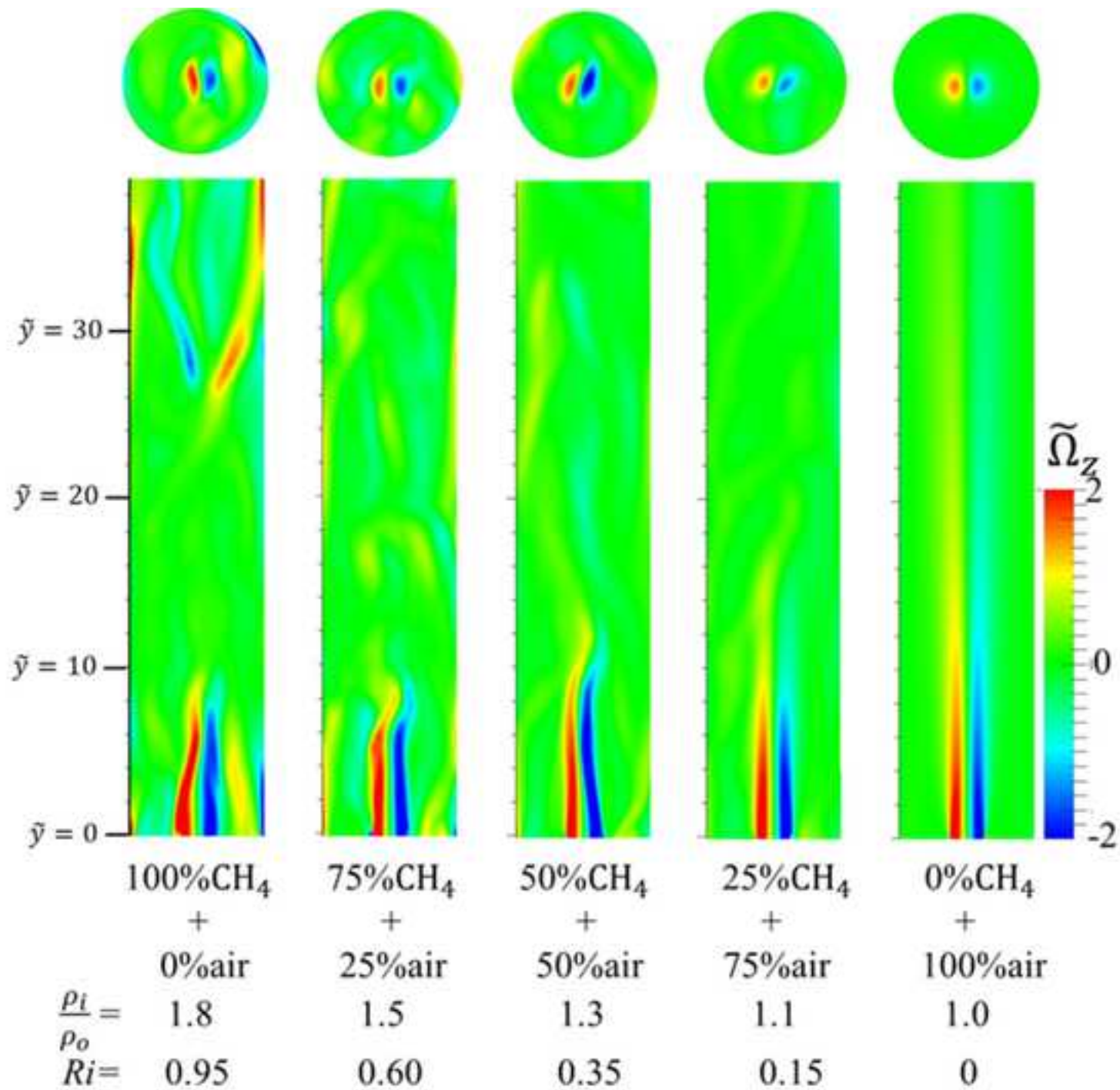


Figure
[Click here to download high resolution image](#)

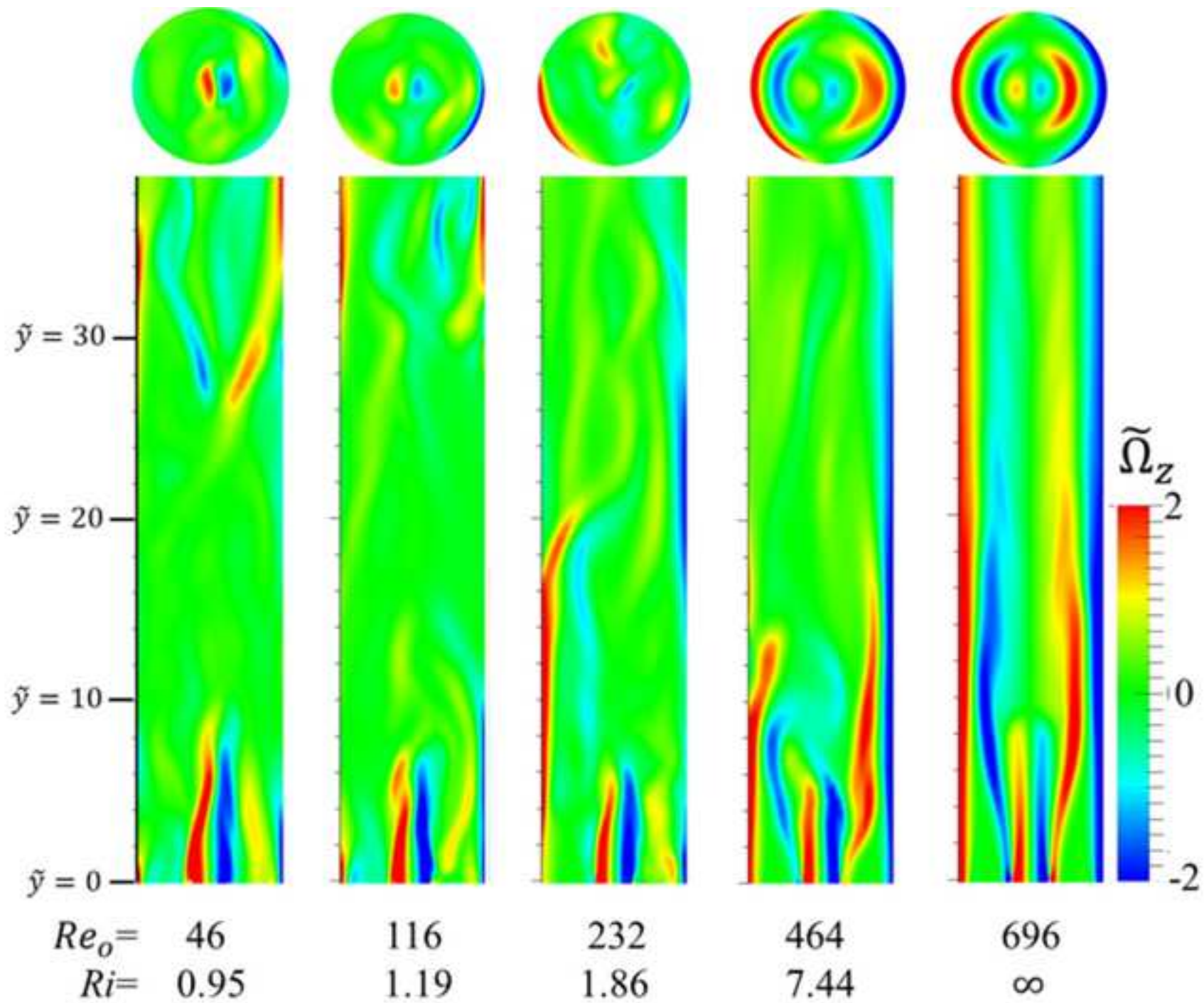
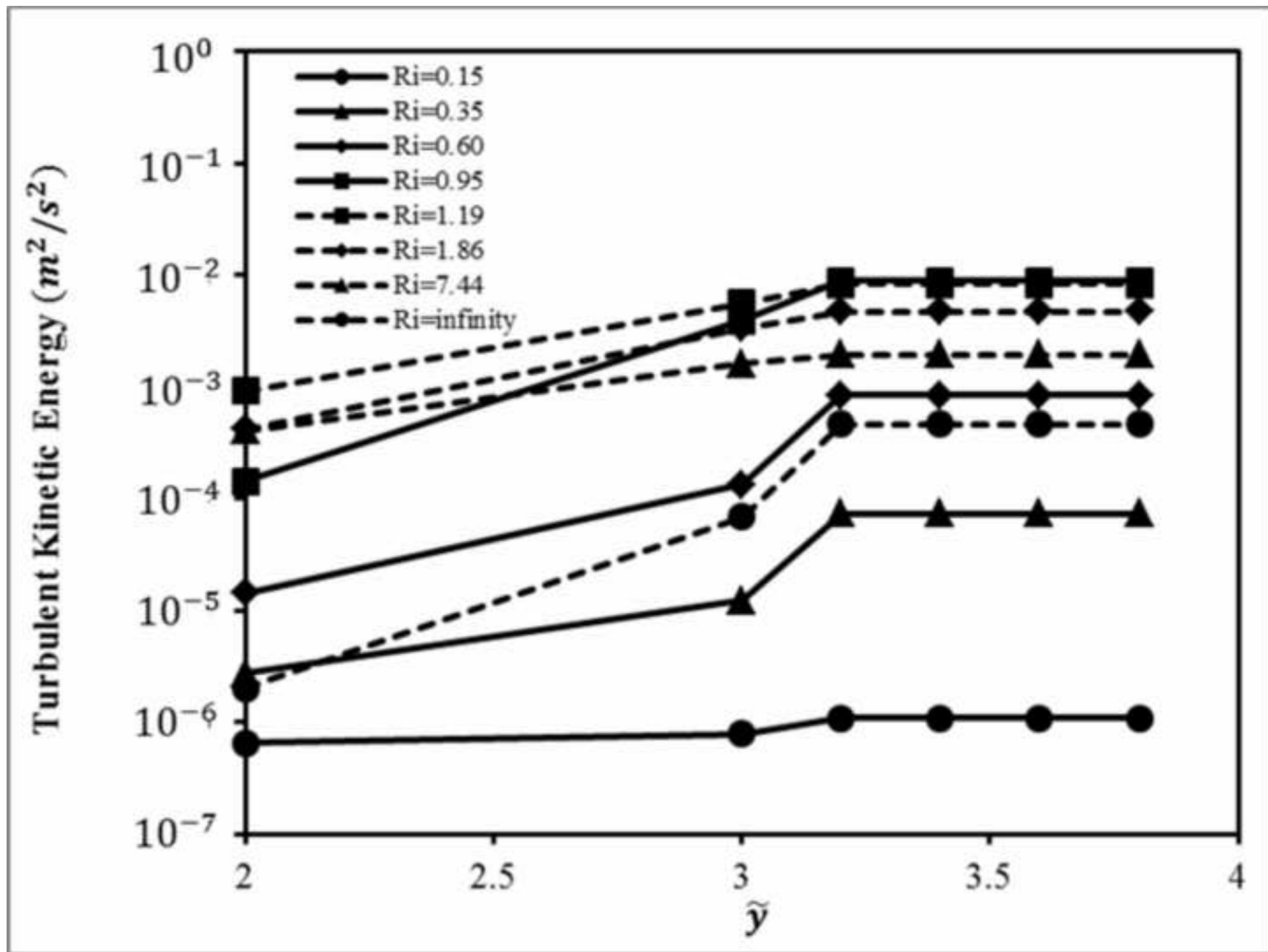
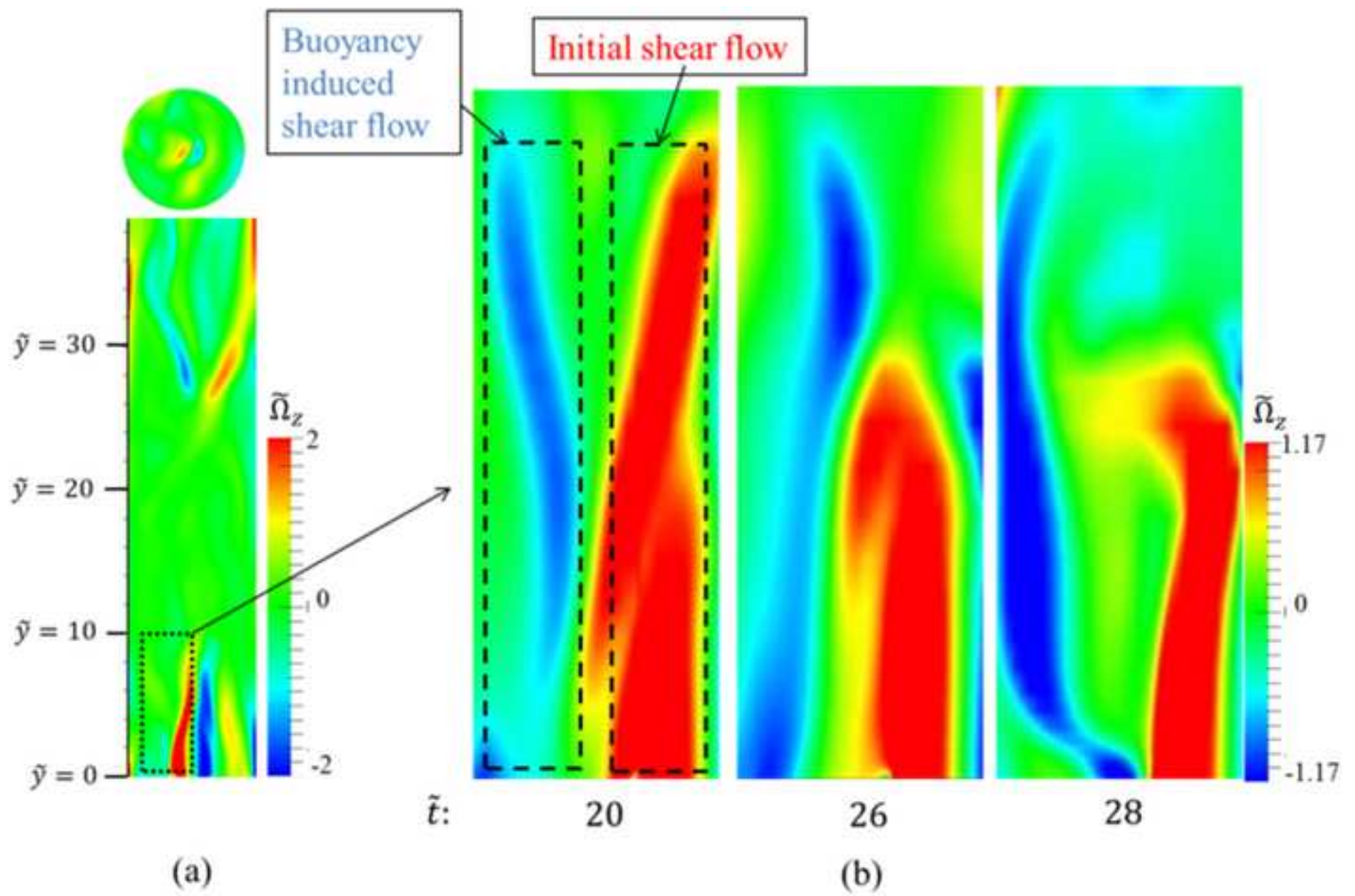


Figure
[Click here to download high resolution image](#)



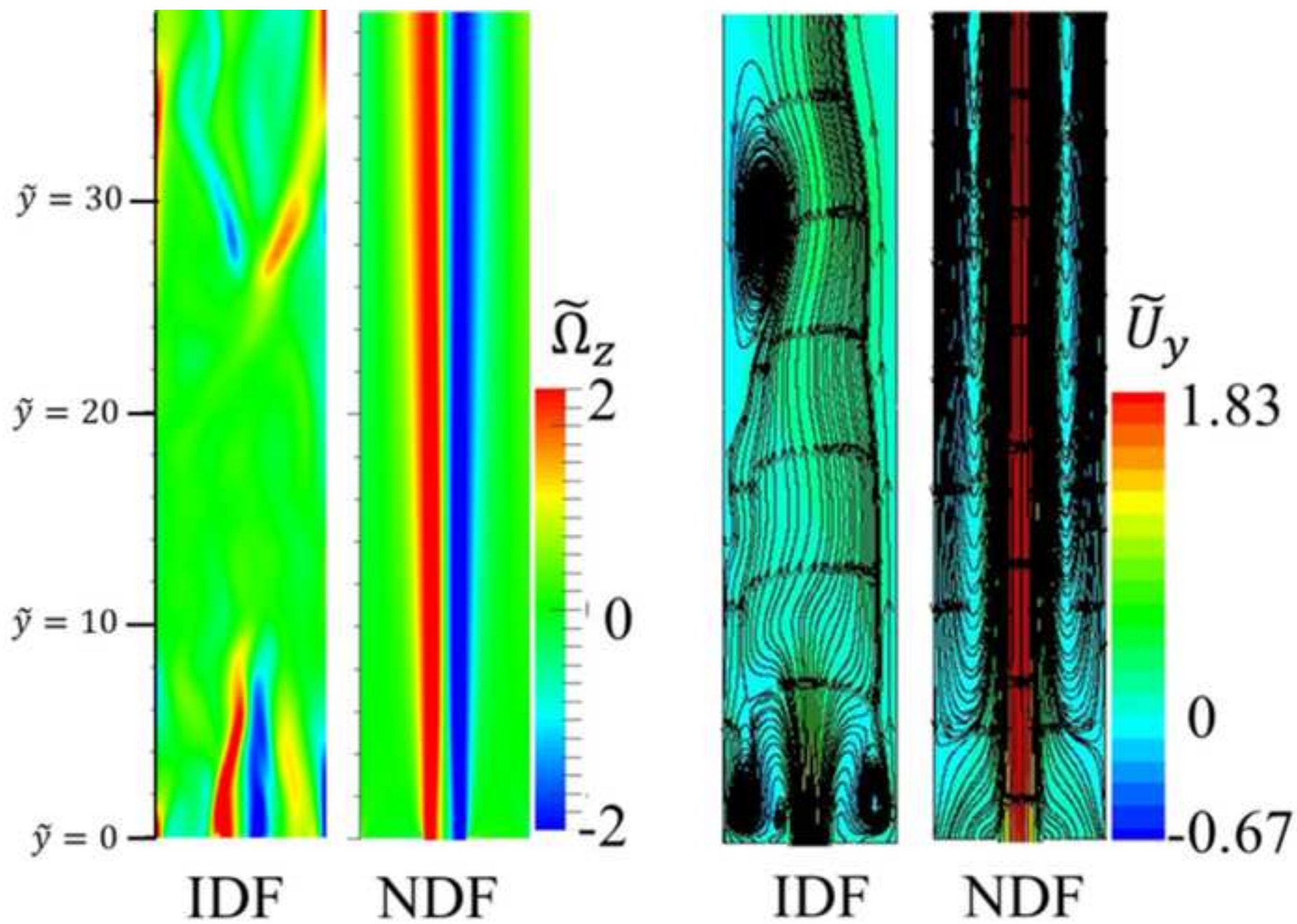
Figure

[Click here to download high resolution image](#)



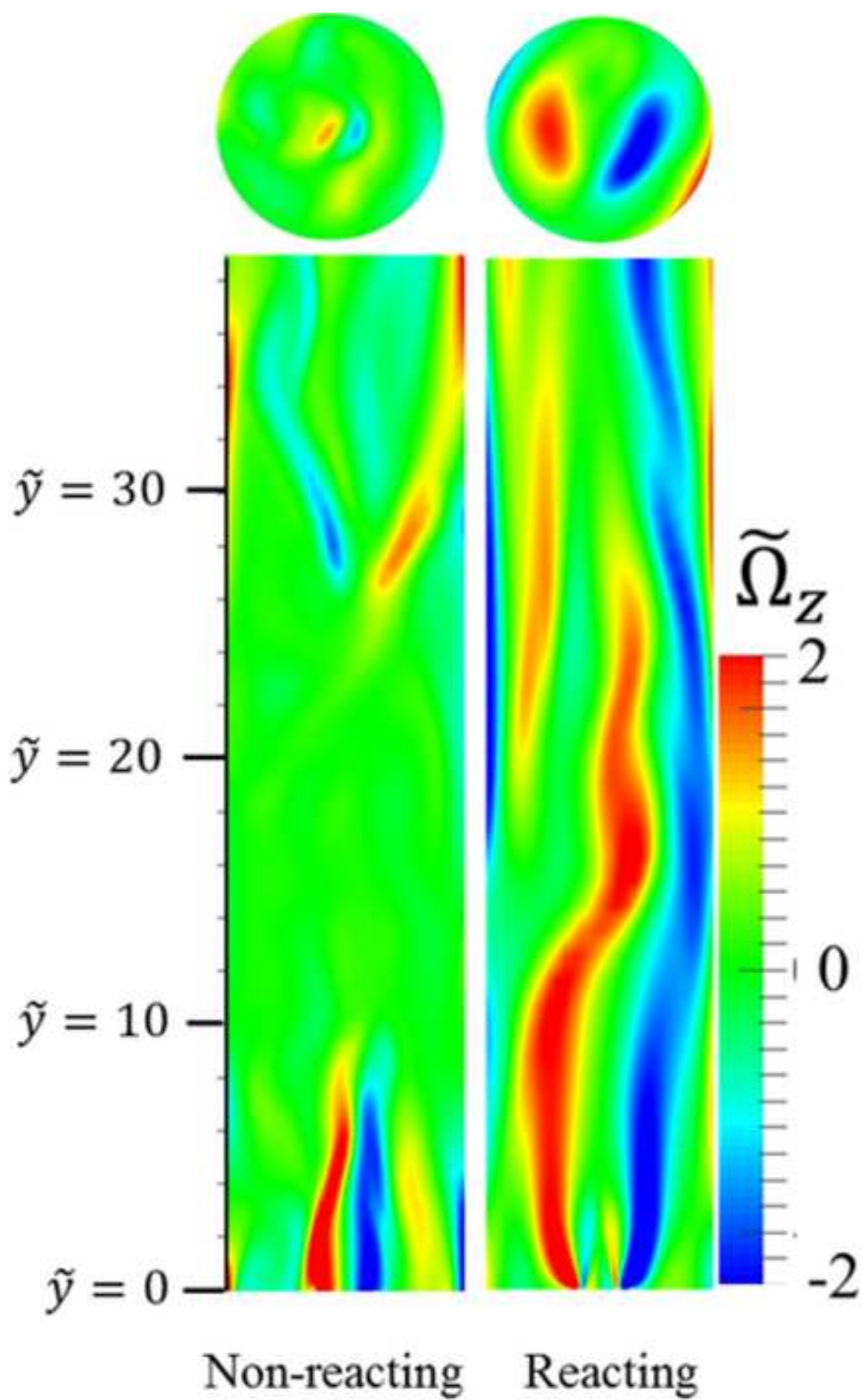
Figure

[Click here to download high resolution image](#)



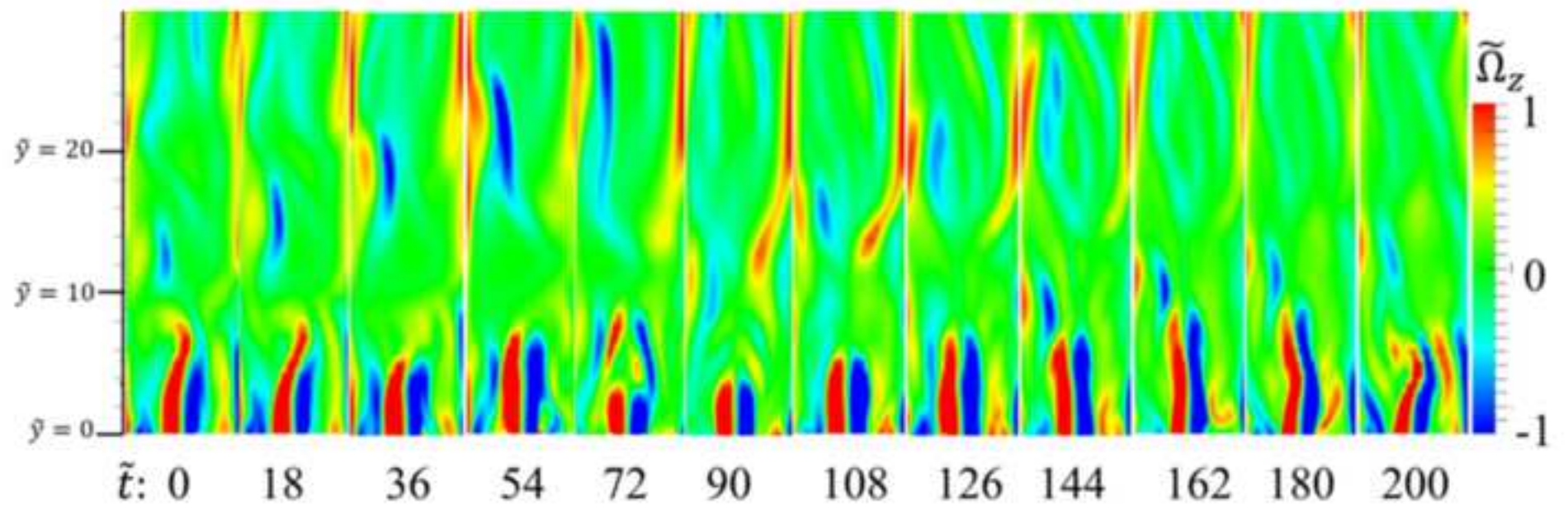
Figure

[Click here to download high resolution image](#)



Figure

[Click here to download high resolution image](#)



Figure

[Click here to download high resolution image](#)

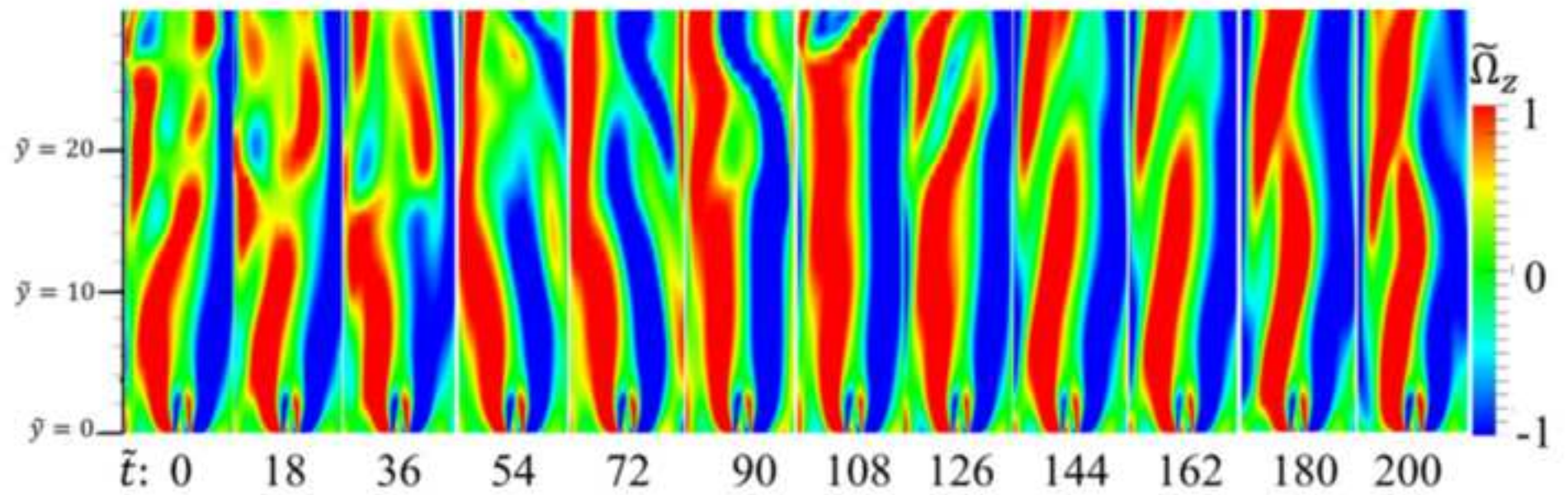


Figure
[Click here to download high resolution image](#)

